EPJ manuscript No.
(will be inserted by the editor)

Review article

New State of Nuclear Matter: Nearly Perfect Fluid of Quarks and Gluons in Heavy Ion Collisions at RHIC Energies

From Charged Particle Density to Jet Quenching

R. Nouicer [a]

Department of Physics, Brookhaven National Laboratory, Upton, NY 11973, United States

Received: date / Revised version: date

Abstract. This article reviews several important results from RHIC experiments and discusses their implications. They were obtained in a unique environment for studying QCD matter at temperatures and densities that exceed the limits wherein hadrons can exist as individual entities and raises to prominence the quark-gluon degrees of freedom. These findings are supported by major experimental observations via measuring of the bulk properties of particle production, particle ratios and chemical freeze-out conditions, and elliptic flow; followed by hard probe measurements: high-$p_{\rm T}$ hadron suppression, dijet fragment azimuthal correlations, and heavy flavor probes. These measurements are presented for particles of different species as a function of system sizes, collision centrality, and energy carried out in RHIC experiments. The results reveal that a dense, strongly-interacting medium is created in central Au + Au collisions at $\sqrt{s_{NN}}$ = 200 GeV at RHIC. This revelation of a new state of nuclear matter has also been observed in measurements at the LHC. Further, the IP-Glasma model coupled with viscous hydrodynamic models, which assumes the formation of a QGP, reproduces well the experimental flow results from Au + Au at $\sqrt{s_{NN}}$ = 200 GeV. This implies that the fluctuations in the initial geometry state are important and the created medium behaves as a nearly perfect liquid of nuclear matter because it has an extraordinarily low ratio of shear viscosity to entropy density, $\eta/s \approx 0.12$. However, these discoveries are far from being fully understood. Furthermore, recent experimental results from RHIC and LHC in small p + A, d + Au and ^{3}He+Au collision systems provide brand new insight into the role of initial and final state effects. These have proven to be interesting and more surprising than originally anticipated; and could conceivably shed new light in our understanding of collective behavior in heavy-ion physics. Accordingly, the focus of the experiments at both facilities RHIC and the LHC is on detailed exploration of the properties of this new state of nuclear matter, the QGP.

PACS. 25.75.-q – Relativistic heavy-ion collisions, 25.75.Ag – Global features, 25.75.Ld – Collective flow, 25.75.Gz – Particle correlations, 25.75.Bh – Hard scattering, 25.75.Nq – Quark–gluon plasma production

arXiv:1512.08993v2 [nucl-ex] 26 Feb 2016

Contents

1 Physics motivation and RHIC achievements 1
2 Global properties of charged hadron production . . 4
2.1 Charged particle density distributions and initial conditions 4
2.2 Particle yields and chemical freeze-out conditions 8
2.3 QGP a nearly perfect fluid 10
2.3.1 Anisotropic particle flow 10
3 Experimental evidence of created dense matter . . . 15
3.1 High-$p_{\rm T}$ hadron suppression: jet-quenching . . 15
3.2 Dijet fragment azimuthal correlations: opaque medium 17
4 Conclusions 19

[a] *rachid.nouicer@bnl.gov*

1 Physics motivation and RHIC achievements

At the heart of each atom, there is a nucleus consisting of distinct nucleons (protons and neutrons). In turn, these nucleons consist of quarks bound together by the strong interaction, mediated by the exchange of gluons. Quantum Chromodynamics (QCD) is considered the fundamental theory for such strong interactions. According to QCD, at ordinary temperatures or densities this force simply confines the quarks into composite particles (hadrons) of around 10^{-15} m = 1 fm in size (corresponding to the QCD energy scale $\Lambda_{\rm QCD} \approx 200$ MeV); its effects are not noticeable at longer distances. However, when the temperature reaches the QCD energy scale (T of the order of 10^{12} Kelvin) or its density rises to the point where the

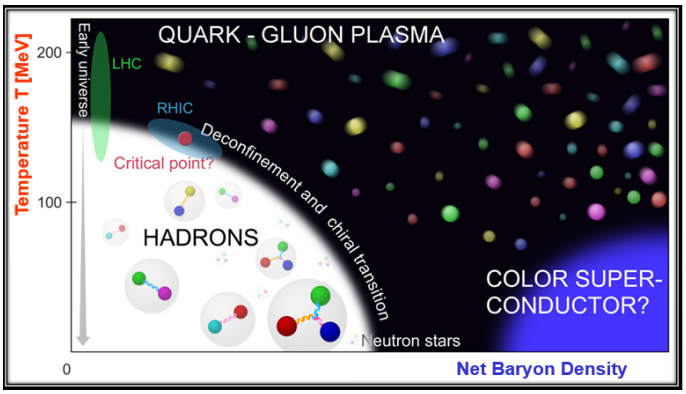

Fig. 1. The phase diagram of QCD matter showing the possible states of quarks. Ordinary matter lies at the bottom left corner, where the temperature and the density of matter both are relatively low. Researchers at the RHIC and LHC explore much higher energies; currently RHIC's researchers are hunting for the possible existence of a critical point at which stable hadrons may mingle with the quark-gluon plasma. This figure is adapted from Ref. [4].

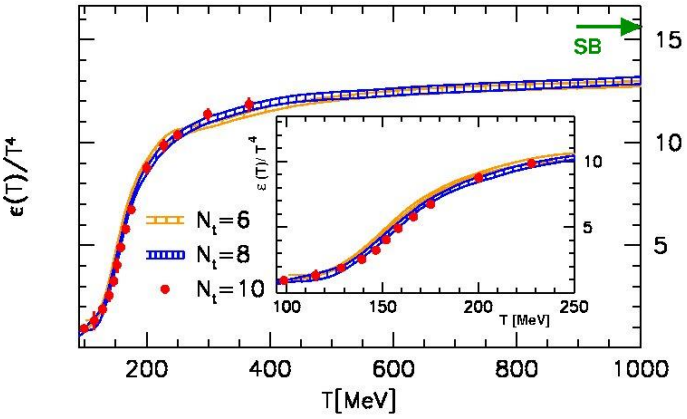

Fig. 2. The energy density normalized by T^4 as a function of the temperature on $N_t = 6$, 8 and 10 lattices. An arrow indicates the Stefan-Boltzmann limit $\varepsilon_{SB} = 3\ p_{SB}$ (see text for details). This figure is adapted from Ref. [5].

average inter-quark separation is less than 1 fm (quark chemical potential μ_q around 400 MeV), hadronic matter under extremely dense and hot conditions undergoes a phase transition to form a Quark Gluon Plasma (QGP) in which quarks and gluons no longer are confined to the size of a hadron [1,2]. Knowing the exact nature of quark confinement in hadrons is crucial, and yet this remains a poorly understood aspect of the quark-gluon description of matter. The QGP is believed to have existed during the first microseconds after the Big Bang [3], and an understanding of its properties could provide valuable insights on the evolution of our Universe. Figure 1 presents the phase diagram of QCD matter, showing the possible states adopted by quarks and gluons [4].

Understanding the properties of strongly interacting matter at high temperatures has been a central goal of many researchers' numerical simulations of lattice QCD. Figure 2 presents recent results from lattice QCD calculations, wherein the energy density is normalized by temperature (T^4) as a function of temperature for a system of $n_f = 2 + 1$ flavors of dynamical quarks [5,6,7]. These calculations reveal a rapid increase in the number of degrees of freedom associated with this deconfinement of quarks and gluons from the hadronic chains. The transition point is at a temperature $T_c = 154 \pm 9$ MeV and energy density $\epsilon_c = 0.18$ to 0.5 GeV/fm^3 [7]. At higher temperatures above the transition, the energy density is still seen to fall about 14% below the ideal Stefan-Boltzmann value for a non-interacting quark/gluon gas (as shown by the arrow), indicating some strong self-interaction remaining at these temperatures. Therefore, scientists have experimentally searched for the signatures both of QGP formation and the in-medium effects of hadron properties. It was proposed that the required high densities could be achieved via relativistic heavy-ion collisions [8]. Over the last decades, relativistic heavy-ion collisions have been studied experimentally at increasingly high center-of-mass energies at the Brookhaven Alternating Gradient Synchrotron (AGS, $\sqrt{s_{NN}} < 5$ GeV), the CERN Super Proton Synchrotron (SPS, $\sqrt{s_{NN}} \leq 20$ GeV), and presently, at the Brookhaven Relativistic Heavy Ion Collider (RHIC, $\sqrt{s_{NN}} \leq 200$ GeV) and the Large Hadron Collider (LHC at CERN, $\sqrt{s_{NN}} = 2.76$ TeV). Simple estimations of the initial energy densities expected for RHIC collisions [9] are many times higher than the threshold for QGP formation from the aforementioned lattice estimations.

For instance, under the RHIC project, an accelerator was constructed at Brookhaven National Laboratory (BNL) from 1991 to 1999. RHIC was designed as a heavy-ion machine, able to provide collisions over a large range of energies. We have attained collisions of gold-gold (Au + Au), copper-copper (Cu + Cu), uranium-uranium (U + U), copper-gold (Cu + Au), deuteron-gold (d + Au), helium-gold (^{3}He + Au), proton-gold (p + Au) and proton-Aluminum (p + Al) at center of mass energies from $\sqrt{s_{NN}} = 7.7$ to 200 GeV. Furthermore, a polarized capability was added to RHIC allowing transverse and longitudinal polarized protons to collide at energies from $\sqrt{s_{NN}} = 62.4$ to 510 GeV. Researchers at RHIC have made a major physics discovery, namely the creation of a new form of matter in high-energy central gold–gold collisions. This matter, dense and strongly interacting, is called the strongly coupled quark-gluon plasma, or sQGP. This finding of a new form of matter was published in four independent white papers [10,11,12,13] from the four RHIC experiments: BRAHMS (Broad RAnge Hadron Magnetic Spectrometers), PHENIX (Pioneering High Energy Nuclear Interaction eXperiment), PHOBOS (not an acronym) , and STAR (Solenoidal Tracker At RHIC). RHIC's accelerator also met and exceeded its specifications; namely, it attained its energy goals and exceeded both the heavy-ion [14,15] and polarized proton [15,16] luminosity. The former luminosity is more than a factor of 25 [14,15] greater than that originally designed. Table 1 summarizes the achievements of RHIC accelera-

tor over the years [15]. Without a doubt, the physics program at RHIC has enabled remarkable advances in the study of hot strongly interacting matter [10,11,12,13,17]. The extended particle momentum range at RHIC allowed the use of hard probes to study the behavior of the created medium that was difficult to access at lower collision energies. The hard penetrating probes now are one of the major experimental tools successfully exploited by RHIC and LHC Collaborations [10,13,18,19]. It should also be pointed out that, recently, new physics results have emerged due to the availability of higher colliding beam energies at the LHC. For example, the studies of two-particle azimuthal correlation functions in the highest-multiplicity $p+p$ collisions at the LHC show an enhancement of particle pair production at relative azimuth $\Delta\phi \simeq 0$, producing a "ridge" structure at the near-side [20]. However, in peripheral $p+\mathrm{Pb}$ collisions, in which only a few nucleons take part and are nominally similar to $p+p$ collisions, a ridge structure is observed on the away-side ($\Delta\phi \simeq \pi$) [21]. The different results between $p+p$ and peripheral $p+\mathrm{Pb}$ collisions are possibly caused by contributions from nuclear effects. In central $p+\mathrm{Pb}$ collisions, a double ridge structure is observed, which is consistent with $\mathrm{Pb}+\mathrm{Pb}$ collisions [22,23]. Another result in the LHC energy regime, $\mathrm{Pb}+\mathrm{Pb}$ collisions at $\sqrt{s_{NN}} = 2.76$ TeV, is the nuclear modification factor $R_{AA}(p_{\mathrm{T}})$ of inclusive J/ψ production measured in the dielectron channel as a function of centrality [19]. These results are compared with the inclusive J/ψ $R_{AA}(p_{\mathrm{T}})$ measured at mid-rapidity by PHENIX in $\mathrm{Au}+\mathrm{Au}$ collisions at $\sqrt{s_{NN}} = 200$ GeV [24]. The inclusive J/ψ production in $\mathrm{Pb}+\mathrm{Pb}$ collisions show less suppression compared to results at RHIC energies, and this behavior is in qualitative agreement with a regeneration scenario at LHC energies [25,26].

In this article, we highlight the RHIC results underlying the major experimental observations from the heavy-ion program, i.e., the identification of a new form of nuclear matter. This required the acquisition of novel and uniquely different measurements from those seen before in heavy-ion collisions at lower energies. To set the foundation, we have focused this review paper on measurements for different particle species as a function of: 1) system size, 2) collision centrality, and 3) energy, all carried out in RHIC experiments. As RHIC is currently still operational, some data presented here has not been available to authors of past review articles. As such the importance of this common set of observables, with a clear interpretation across the broad system size and beam energies, presented here may not have been emphasized. These findings are supported by major empirical observations and elucidated in the present work from both soft and hard probe sectors. For soft probes, measurements on the production of bulk particles and the initial conditions are presented, followed by particle ratios and chemical freeze-out conditions. These measurements are very important as they support the characterization of the system produced in such collisions and provide basic constraints to theoretical models. To complete the soft-sector discussion, we present measurements of collective flow that are related in-

Table 1. RHIC operating modes and total integrated luminosity delivered to all experiments for each run [15].

Run	Species	Total particle energy: $\sqrt{s_{\mathrm{NN}}}$ [GeV/nucleon]	Total delivered luminosity [$\mu\mathrm{b}^{-1}$]
I (2000)	Au+Au	56	< 0.001
	Au+Au	130	20
II (2001/2002)	Au+Au	200	258
	Au+Au	19.6	0.4
	p+p	200	1.4×10^{-6}
III (2003)	d+Au	200	73×10^{-3}
	p+p	200	5.5×10^{-6}
IV (2004)	Au+Au	200	3.53×10^{-3}
	Au+Au	62.4	67
	p+p	200	7.1×10^{-6}
V (2005)	Cu+Cu	200	42.1×10^{-3}
	Cu+Cu	62.4	1.5×10^{-3}
	Cu+Cu	22.4	0.02×10^{-3}
	p+p	200	29.5×10^{-6}
	p+p	410	0.1×10^{-6}
VI (2006)	p+p	200.0	88.6×10^{-6}
	p+p	62.4	1.05×10^{-6}
VII (2007)	Au+Au	200.0	7.25×10^{-3}
	Au+Au	9.2	small
VIII (2008)	d+Au	200	437×10^{-3}
	p+p	200	38.4×10^{-6}
	Au+Au	9.2	small
IX (2009)	p+p	500	110×10^{-6}
	p+p	200	114×10^{-6}
X (2010)	Au+Au	200	10.3×10^{-3}
	Au+Au	62.4	544
	Au+Au	39	206
	Au+Au	7.7	4.23
	Au+Au	11.5	7.8
XI (2011)	p+p	500	166×10^{-6}
	Au+Au	19.6	33.2
	Au+Au	200	9.79×10^{-3}
	Au+Au	27	63.1
XII (2012)	p+p	200	74.0×10^{-6}
	p+p	510	283×10^{-6}
	U+U	193	736
	Cu+Au	200	27.0×10^{-3}
XIII (2013)	p+p	510	1.04×10^{-9}
XIV (2014)	Au+Au	14.6	44.2
	Au+Au	200	43.9×10^{-3}
	He+Au	200	134×10^{-3}
XV (2015)	p+p	200	382×10^{-6}
	p+Au	200	1.27×10^{-6}
	p+Al	200	3.97×10^{-6}

directly to the thermodynamical or hydrodynamical properties of the new form of nuclear matter, a nearly perfect fluid. This discussion is then followed by hard probe measurements: high-$p_{\rm T}$ hadron suppression and dijet fragment azimuthal correlations which lead to the observation of the jet quenching in relativistic heavy-ion collisions viz., one of the most remarkable discoveries at RHIC. These measurements of hard probes afford experimental evidence of highly interacting dense matter created in central Au + Au collisions at $\sqrt{s_{_{NN}}} = 200$ GeV. Interpretation of the modification of bound states of heavy quarks, charmonium and bottomonium, is heavily impacted by many competing effects in heavy ion collisions including large initial state nuclear effects not directly related to the formation of the quark-gluon plasma and a full understanding of these observables has not yet been formulated [27,28,29,30]. This review of hard sector observables thus focuses on quenching observables which are more simply related to the properties of the quark-gluon plasma. Global properties of charged hadron production including the empirical evidence of QGP a nearly perfect fluid are presented in Section 2. Experimental observations of the creation of dense medium, and its opacity, based on high-$p_{\rm T}$ hadron suppression, and dijet fragment azimuthal correlations are elucidated in details in Section 3.

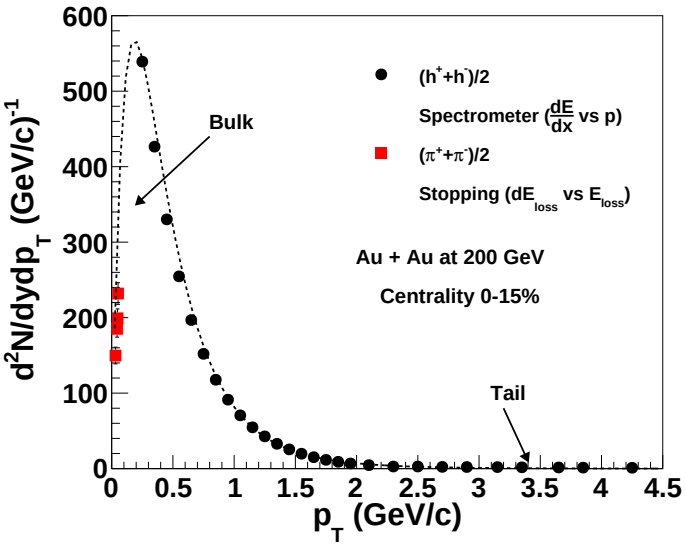

Fig. 3. The measured distribution of charged hadrons as a function of transverse momentum, $p_{\rm T}$, for the 0-15% most central Au + Au collisions at $\sqrt{s_{_{NN}}} = 200$ GeV [31].

2 Global properties of charged hadron production

The heavy-ion collisions at the highest RHIC energy, i.e. Au + Au at $\sqrt{s_{_{NN}}} = 200$ GeV, heralded a new era of opportunities for studying hadronic matter under conditions of high energy density. The theory of strong interactions, QCD, can be used to compute processes perturbatively in the limit of short distances. At present, however, we cannot compute, from first principles, many interesting quantities at large distance. Therefore, it is important to characterize the collisions using global extrinsic observables. Measurements of charged hadron multiplicity and transverse energy distributions and collective flow in heavy-ion collisions afford us information on the initial energy density, initial collision geometry and the entropy production during the system's evolution. All are sensitive to a variety of physics processes responsible for multi-particle production. This knowledge is important for constraining model predictions and indispensable for understanding and estimating the accuracy of the more detailed measurements, for example, those of jets or quarkonia production.

Figure 3 shows the measured transverse momentum, $p_{\rm T}$, distribution of charged hadrons produced in the 0-15% most central Au + Au collisions at $\sqrt{s_{_{NN}}} = 200$ GeV [31]. The distribution illustrates a "bulk" and "tail" respectively often associated to "soft" and "hard" parton-parton scattering. However, there is no clear separation between "soft" and "hard" processes. For this reason, we require an analysis undertaken as a function of centrality, transverse momentum, energy, and system sizes to better understand particle production. We note that most of the particles under investigation correspond to "thermal" pions ($p_{\rm T} < 2$ GeV/c) and, in general, such thermal hadrons make up about 95% of the observed particle multiplicity referred to as the bulk of hadron production. Their distribution in phase space of pseudorapidity (η) as a function of collision centrality and energy is presented in Subsection 2.1. These measurements led to the first insights into the overall reaction dynamics, and also set the stage for considering more rare signals, embedded in this thermal bulk production.

2.1 Charged particle density distributions and initial conditions

One important observable in heavy-ion interactions is the charged particle pseudorapidity density, $\mathrm{dN_{ch}/d}\eta$. The pseudorapidity, η, is defined as $\eta = -\ln[\tan(\theta/2)]$, where θ is the emission angle relative to the direction of the beam. This quantity ($\mathrm{dN_{ch}/d}\eta$) is proportional to the entropy density at freeze-out. Since the entropy density of a closed system will be non-decreasing [32], the pseudorapidity density provides information on the partons' initial-state density and any further entropy produced during subsequent evolution [33]. In describing the collision of two nuclei, several variables are used to quantify the collision's centrality including, the number of participants nucleons (number of interacting nucleons), $\mathrm{N_{part}}$, and the number of binary collisions (number of nucleon-nucleon collisions), $\mathrm{N_{coll}}$. Both are given in terms of the impact parameter, b (see Figs. 4 and 12(a)), the distance between the centers of two colliding nuclei. A small value of b corresponds to more central collisions, whilst a large value to peripheral collisions. The impact parameter is not directly measurable but experiments at BNL (AGS, RHIC) and CERN (SPS, LHC)

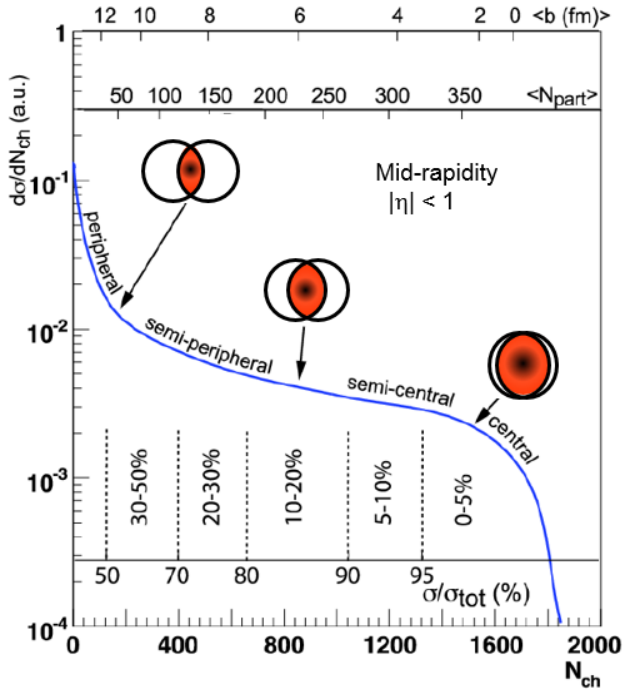

Fig. 4. Schematic diagram of a distribution of a centrality variable, i.e. the number of charged particles in the interval $|\eta| < 1$. The events contributing to the upper 5% of the integral of the distribution are the 0-5% centrality bin, with a near complete nuclear overlap. The parameters from a Glauber simulation, $\langle b \rangle$, $\langle N_{part} \rangle$, are shown as different horizontal scales. This figure is adapted from Ref. [36].

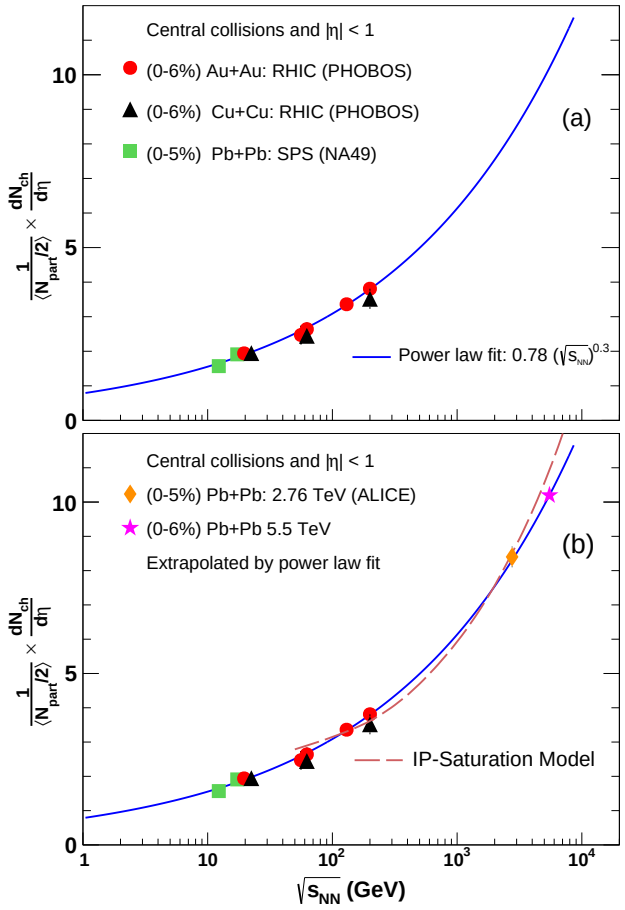

Fig. 5. The measured scaled pseudorapidity density $dN_{ch}/d\eta/\langle \frac{1}{2} N_{part} \rangle$ for $|\eta| < 1$ in central $Au + Au$, $Cu + Cu$ and $Pb + Pb$ collisions at the SPS, RHIC and LHC energies [33,38,39,40,41,42,43,44]. The star symbols denote the extrapolation in central $Pb + Pb$ collisions at 5.5 TeV (LHC). The error bars show the systematic errors. The solid curve corresponds to the power law fit of the RHIC data. The Impact Parameter dipole saturation model (IP-saturation model) calculation from RHIC to LHC is illustrated by a dashed curve [45]. See text for details

showed that the relation between number of charged particles produced (and the energy of the produced particles in the transverse direction, E_T) and on average the number of nucleon participants, $\langle N_{part} \rangle$, is monotonic. Thus, since the dependence of N_{part} on the impact parameter can be calculated with some precision for a given nuclear density distribution, we can get a handle on the collision's centrality. The Glauber model is a semi-classical model picturing nucleons with fixed transverse positions moving in the collision direction in a straight path [34,35]. It provides a geometrical description of multiple nucleon collisions, and is used to relate the impact parameter to the number of participants and the number of N+N collisions, based on the assumption of constant inelastic cross section for each subsequent collision. Figure 4 shows the minimum-bias multiplicity (N_{ch}) distribution used for selecting collision centrality. The minimum-bias yield was cut into successive intervals, starting from the maximum value of N_{ch}. The first 5% of the high N_{ch} events correspond to the top 5% central collisions. The relationship of centrality and impact parameter with the number of participating nucleons was elaborated in Glauber-type Monte Carlo calculations employing the Wood-Saxon nuclear density distributions [36,37].

Figure 5(a) shows the measured densities of charged particle near the mid-rapidity region, $dN_{ch}/d\eta|_{|\eta|<1}/\langle N_{part}/2 \rangle$, as a function of center–of–mass collision energy ($\sqrt{s_{NN}}$) for $Au + Au$ (RHIC: $\sqrt{s_{NN}}$ = 19.6, 56, 62.4, 130 and 200 GeV), and $Cu + Cu$ (RHIC: $\sqrt{s_{NN}}$ = 22.4, 62.4 and 200 GeV) [33,38,39,40,41]. The measurements present the 0-6% most central collisions at mid-rapidity region and $\langle N_{part} \rangle$ is the average number of participant nucleon pairs, for $Au + Au$ and $Cu + Cu$. The results (see Fig. 5(a)) suggest that the particle density rises approximately logarithmically with energy. Comparing the findings for $Au + Au$ and $Cu + Cu$ indicates that, for the most central events in symmetric nucleus-nucleus collisions, the particle density per nucleon participant pair does not depend on the size of the two colliding nuclei but only on the energy of the collision [40,41]. For comparison, the RHIC data is compared to those obtained at the CERN SPS for $Pb + Pb$ collisions at $\sqrt{s_{NN}}$ = 12.3 and 17.3 GeV [42,43]. We observe that at maximum RHIC energy, $\sqrt{s_{NN}}$ = 200 GeV,

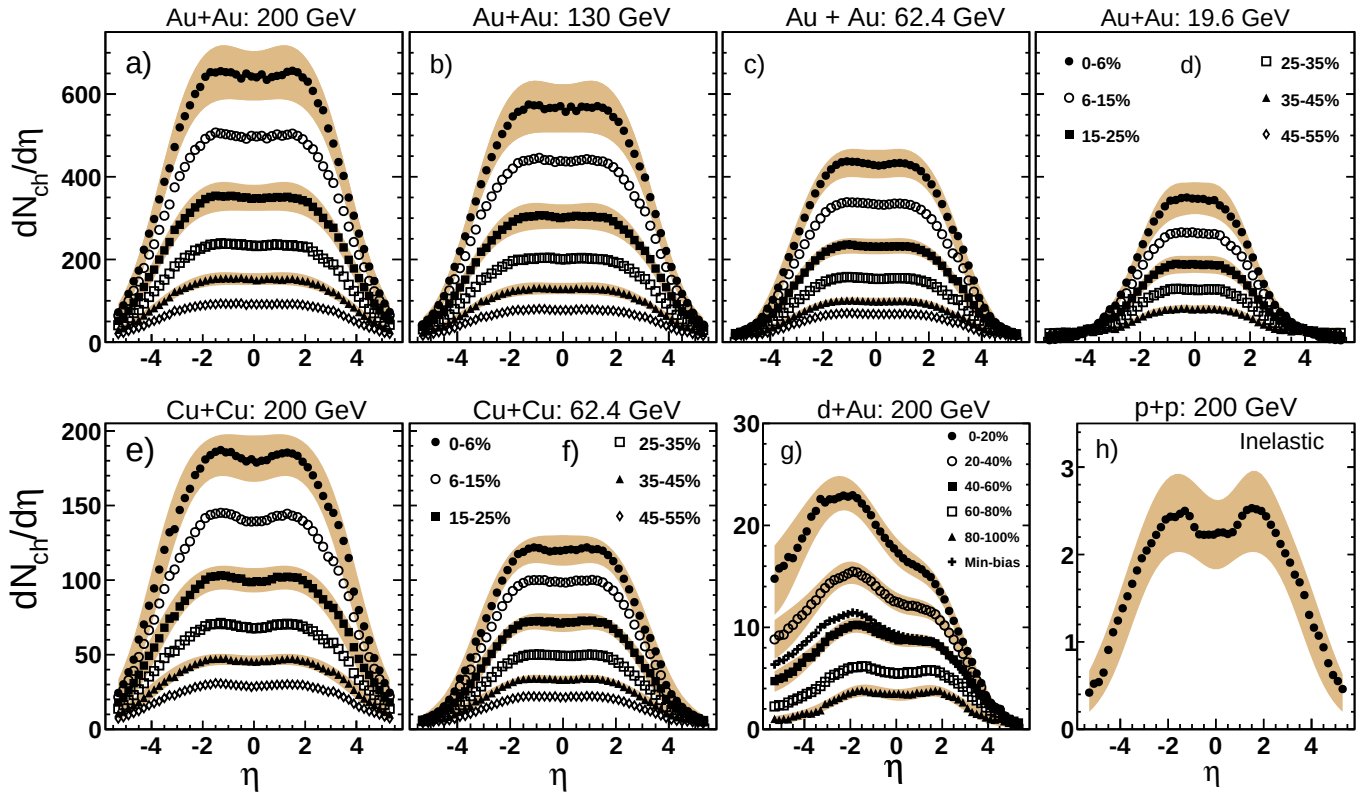

Fig. 6. The measured pseudorapidity density distributions of charged particles produced in Au + Au, Cu + Cu, d + Au, and $p + p$ collisions at RHIC energies. The $dN_{ch}/d\eta$ distributions for Au + Au, Cu + Cu and d + Au collisions are plotted as a function of the collision's centrality. Typical systematic errors are represented as bands for selected centrality bins. The statistical errors are negligible [38,33,39,40,41].

is a 98% higher particle density per participant pair in near $\eta = 0$ than at the maximum SPS energy, 17.3 GeV. General arguments based on Bjorkens estimate [9] suggest that this increase should correspond to a similar increase in the maximal energy density achieved in the collision.

Based on the Au + Au data in Fig. 5(a) obtained at RHIC energies, one can establish a power law fit to predict (extrapolate) the results of $dN_{ch}/d\eta$ at the mid-rapidity region ($|\eta| < 1$) to Pb + Pb central collisions at the LHC's energy 5.5 TeV. The power law fit to the RHIC data is shown as the solid curve in Fig. 5(a) and 5(b).
The corresponding of the power law fit function is:

$$f_{AA}^{Pow} = 0.78 \times (\sqrt{s_{NN}})^{0.3}. \quad (1)$$

The $\sqrt{s_{NN}}$ is in GeV unit. We observe that the power law fit has a good agreement with the SPS and RHIC data, allowing one to extrapolate the scaled density per nucleon participant pair for 0-6% central Pb + Pb collisions at LHC energy, 5.5 TeV, in the mid-rapidity region ($|\eta| < 1$):

$$f_{AA}^{Pow}(5.5\ \text{TeV}) = \frac{1}{\langle N_{part}/2\rangle}\frac{dN_{ch}}{d\eta}(\text{Pb} + \text{Pb at } 5.5\ \text{TeV})$$
$$f_{AA}^{Pow}(5.5\ \text{TeV}) = 10.3 \pm 0.26$$

where the uncertainties are propagated from the power law fit parameters. Using a Glauber model calculation for the 0-6% most central Pb + Pb collisions at 5.5 TeV (the total inelastic cross section used in the Glauber model calculation is $\sigma_{NN} = 72$ mb), a value of $\langle N_{part}\rangle = 381 \pm 11$ is obtained, from which the unscaled charged particle pseudorapidity density, i.e. using the power law extrapolation, at mid-rapidity ($|\eta| < 1$) can be deduced:

$$\frac{dN_{ch}}{d\eta}(6\%\ \text{central, Pb} + \text{Pb at } 5.5\ \text{TeV}) = 1962\ \pm 50$$

The results from ALICE (A Large Ion Collider Experiment) at LHC [44] on charged particles density at mid-rapidity region and for 0-5% most central Pb + Pb collisions at $\sqrt{s_{NN}} = 2.76$ TeV corresponds to the following:

$$\frac{1}{\langle N_{part}/2\rangle} \times \frac{dN_{ch}}{d\eta}(\text{Pb} + \text{Pb at } 2.76\ \text{TeV}) = 8.4 \pm 0.3$$

As shown in the Fig. 5(b), the power law fit function and the ALICE/LHC results for central Pb + Pb at 2.76 TeV agree with this extrapolated trend.

The calculations of the Impact Parameter dipole Saturation model (IP-Sat model) [45] for charged particle density, $dN_{ch}/d\eta|_{|\eta|<1}/\langle N_{part}/2\rangle$, as a function of energy from

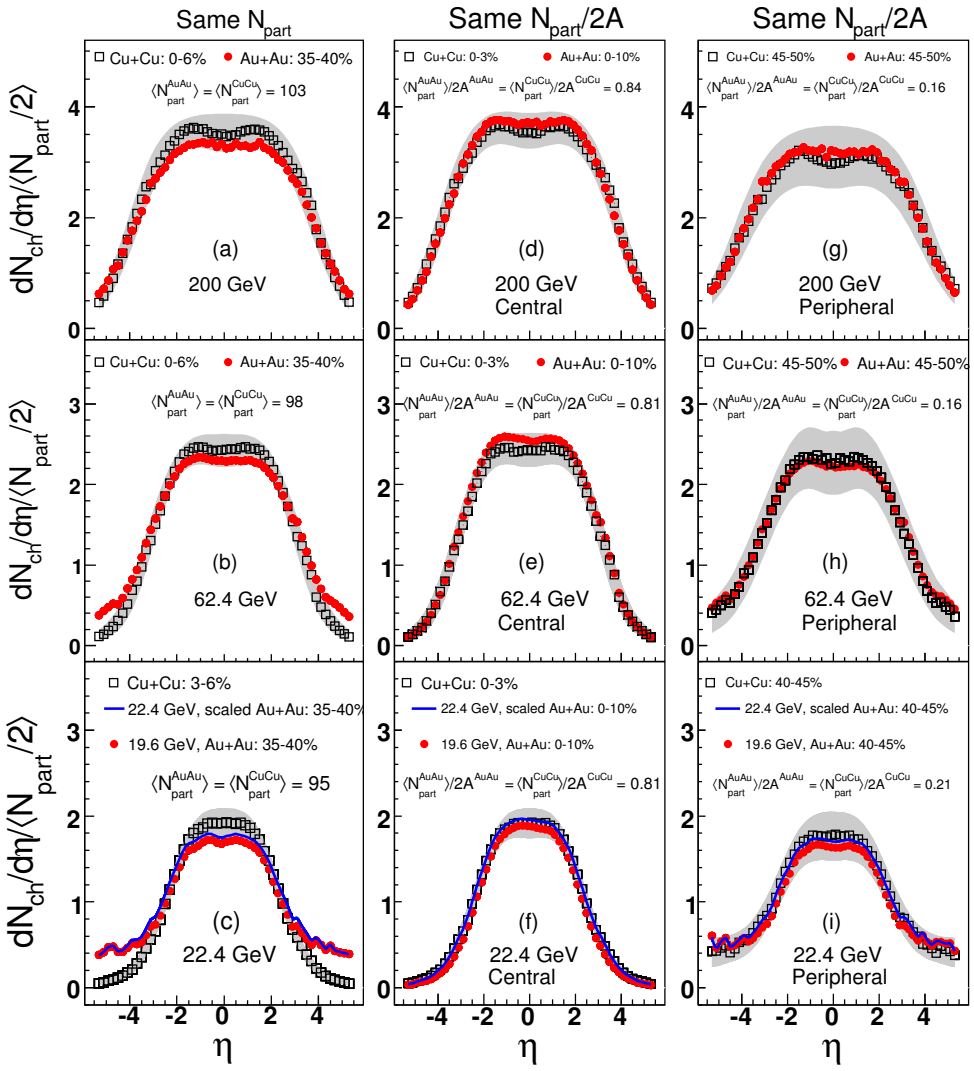

Fig. 7. The measured $dN_{ch}/d\eta/\langle N_{part}/2\rangle$ distributions in Cu + Cu and Au + Au collisions at 22.4 (19.6), 62.4 and 200 GeV selected to yield the following: Panels (a)-(c) similar $\langle N_{part}\rangle$, panels (d)-(f) central collisions with similar volume of overlap region, $\langle N_{part}\rangle/2A$ and panels (g)-(i) peripheral collisions with similar volume of overlap region (i.e., the fraction of the total nuclear volume that interacts), $\langle N_{part}\rangle/2A$. The band indicates the systematic uncertainty for Cu + Cu collisions. For the sake of clarity, the errors for Au + Au are not shown [38,33,39,40,41].

RHIC to LHC are represented in Fig. 5(b) by the dashed curve. We observe that the IP-Sat model is in reasonably good agreement with the data [45]. In these theoretical calculations (IP-Sat model), $dN_{ch}/d\eta$ is estimated to be approximately 2/3 times the initial gluon density, dN_g/dy. Further, this indicates that in IP-Sat model the saturation scale grows roughly as $\langle Q_S^2\rangle \sim (\sqrt{s})^{0.3}$ if a fixed value of $\alpha_s = 0.2$ is assumed as in Ref. [45]. In the Color Glass Condensate (CGC) framework, the produced gluon multiplicity $dN_g/dy \sim \langle Q_S^2 S_\perp\rangle/\alpha_s$ is expected where Q_S^2 is the minimum saturation scale of the two colliding nuclei, and $S_\perp$ is the overlap area [46,47].

Figure 6 shows the measured $dN_{ch}/d\eta$ of primary charged particles over a broad range of pseudorapidity, $|\eta| < 5.4$, for Au + Au [38,33,39] and Cu + Cu [40,41] collisions under a variety of collision centralities and RHIC energies. The data from d + Au [48,49,50] and $p + p$ [48,51] at RHIC energies also are shown. Both the height and width of the $dN_{ch}/d\eta$ distributions increase as a function of energy as observed in the Au + Au and Cu + Cu collisions. The Au + Au, Cu + Cu, d + Au and $p + p$ data at all energies were obtained with the same detector setup in the PHOBOS experiment at RHIC [52,53]. This situation is optimal as common systematic errors cancel each other out in the ratio. With this configuration, we were able to examine comprehensively both particle production in Cu + Cu and the Au + Au collisions for the same N_{part}, for the same fraction of total inelastic cross sections, and for the same geometry in both systems.

Figure 7 presents a comparison of $dN_{ch}/d\eta$ distributions for Au + Au and Cu + Cu collisions at similar energies, $\sqrt{s_{NN}} = 22.4$ (19.6), 64.2 and 200 GeV. The $dN_{ch}/d\eta$

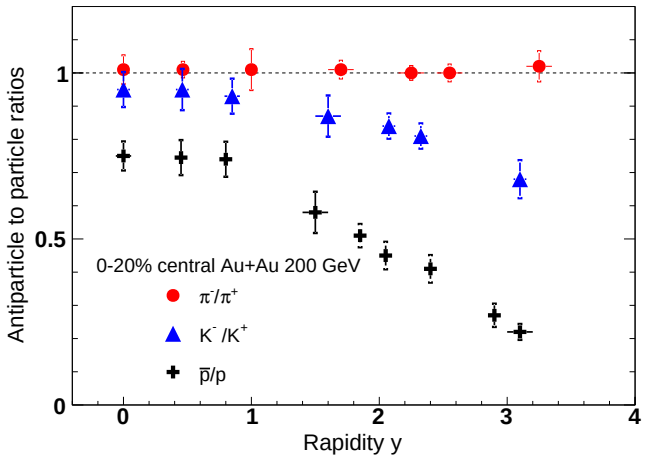

Fig. 8. The measured antiparticle to particle ratios as a function of rapidity in 0-20% central Au + Au collisions at $\sqrt{s_{NN}}$ = 200 GeV. Error bars show the statistical errors while the caps indicate the combined statistical and systematic errors [56].

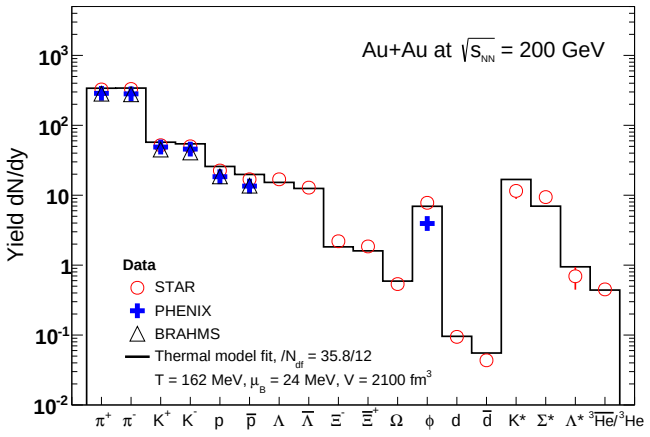

Fig. 9. The experimental hadron yields and statistical thermal model comparison for different particle species produced in central Au + Au at $\sqrt{s_{NN}}$ = 200 GeV [57].

distributions are normalized to N_{part}. The goal from the measurements presented in Fig. 7 is to study the sensitivity of the full shape of the pseudorapidity distributions in Au + Au and Cu + Cu collisions when the overlap collision regions in both systems are selected: (1) for the same number of nucleon participants (N_{part}), and (2) for the same fraction ($N_{part}/2A$), which should reflect the volume of overlap region as a fraction of the total nuclear volume where A is the mass number of the colliding nuclei. The first comparison is made for centrality bins chosen such that the average number of participants in both systems is the same, Fig 7(a)-(c). This comparison reveals that, at 200 GeV, the height and the width of the $dN_{ch}/d\eta$ distributions in both systems agree within systematic errors, and that at 62.4 and 22.4 GeV, the distributions agree within systematic errors at mid-rapidity but not in the fragmentation regions (i.e., high $|\eta|$). The $dN_{ch}/d\eta$ distributions of Au + Au collisions at 19.6 and 62.4 GeV were interpolated linearly in $\ln(\sqrt{s_{NN}})$ to obtain the scaled Au + Au data at 22.4 GeV. We observed that the production of charged particles in the high $|\eta|$ region is increased in Au + Au compared to that in Cu + Cu collisions. This increase may be attributed to the two excited nuclear remnants being bigger in the former collisions relative to the latter. This effect is most visible at the lowest energies where the broad η coverage gives access to $|\eta| > y_{beam}$. The second comparison, Fig. 7(d)-(f), shows $dN_{ch}/d\eta$ distributions in centrality bins with similar values of $N_{part}/2A$ (and automatically have matching $N_{spec}/2A$ values, where N_{spec} = 2A - N_{part} is the number of non-participating nucleons, the spectators) in Au + Au and Cu + Cu systems. We observe a better matching over the full η coverage and for the three energies, 22.4, 62.4, and 200 GeV, see Fig. 7(d)-(f), with the results shown for central collisions in both systems. Similar comparisons (same $N_{part}/2A$) for more peripheral bins lead to the same conclusion as shown in Fig. 7(g)-(i). The comparison presented in the Fig. 7 reveals an interesting feature: the $dN_{ch}/d\eta/\langle N_{part}/2\rangle$ distributions of central Au + Au and central Cu + Cu collisions (as well peripheral Au + Au and peripheral Cu + Cu collisions) are similar over the detector's full coverage ($|\eta| < 5.4$), and for the three energies, 22.4, 62.4 and 200 GeV, implying that the production of charged particles, normalized to the number of nucleon participants, is mostly driven by the volume of overlap region, $N_{part}/2A$ (i.e., the fraction of the total nuclear volume that interacts).

One question is whether the mechanisms in the limiting fragmentation region (i.e. high $|\eta|$) are distinct from those at mid-rapidity region ($|\eta| < 1$). From the results in the Figs. 6 and 7 for the Au + Au, Cu + Cu, d + Au, and $p + p$ collisions, there is no obvious evidence for two separate regions at any of the RHIC energies. However, to date no such anomalies have been noted at the energies of the AGS, SPS, RHIC, or LHC. So far, all results on charged particle pseudorapidity densities point to a rather smooth evolution in centrality, peseudorapidity, and $\sqrt{s_{NN}}$. It had been imagined, that a phase transition would manifest as a non-monotonic behavior in these observables; such sharp features are absent, but that alone does not rule out the presence of a phase transition [54]. It should be noted that mechanisms of charged particle production for $dN_{ch}/d\eta$ (Fig. 6) are mostly driven by "soft" processes (Fig. 3). Also note that pseudorapidity distributions correspond to inclusive measurements of charged hadrons. It would be interesting to have the same measurements for identified particles over a large coverage (i.e. $|\eta| < 5.4$) as the behavior of particles species in the two regions, mid-rapidity and fragmentation, may differ.

2.2 Particle yields and chemical freeze-out conditions

Chemical freeze-out is the stage in the evolution of the hadronic system at which inelastic collisions cease and the

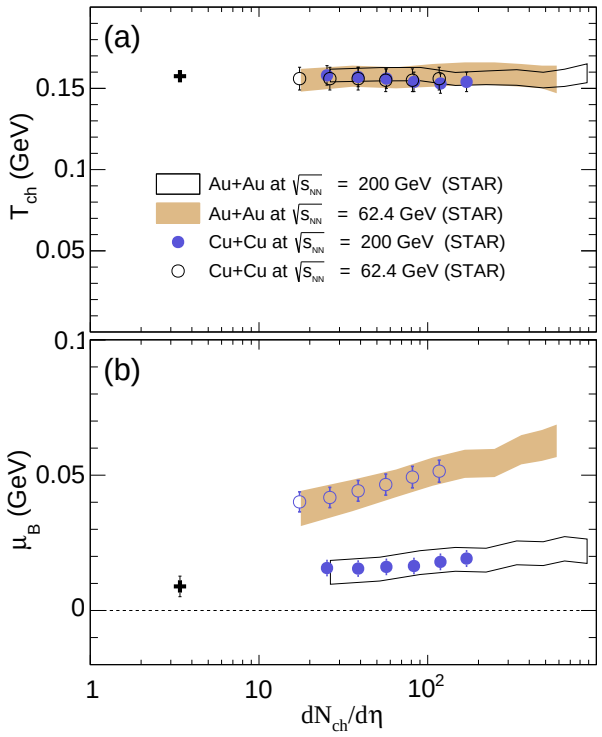

Fig. 10. The chemical freeze-out temperature, T_{ch}, and baryon chemical potential, μ_B, as a function of centrality $dN_{ch}/d\eta$ shown respectively in panels (a) and (b). The data are for $\sqrt{s_{NN}}$ = 200 and 62.4 GeV in Au + Au (bands) and Cu + Cu (symbols). For comparison, the results for minimum-bias $p+p$ collisions at $\sqrt{s_{NN}}$ = 200 GeV are also shown using data from Ref. [59].

relative particle ratios become fixed. In a chemical analysis within the grand-canonical ensemble, the statistical-thermal model with conservation laws requires at least five parameters as input: volume V, the chemical freeze-out temperature T_{ch}, baryon-, strangeness- and charge chemical potentials μ_B, μ_S and μ_Q respectively. These parameters determine the particle composition in the hadronic final state. After chemical freeze-out, the particle composition inside the fireball is fixed, but elastic collisions keep the system interacting until the final, thermal (kinetic) freeze-out. At this stage the produced particle spectra are fixed (modulo weak decays) and carry information about the phase-space distribution in the final state of the fireball. Therefore, the transverse momentum spectra determine the parameters of the thermal freeze-out. Thereafter, statistical interpretation of particle production becomes an appropriate approach for evaluating heavy-ion collisions at high energies because of the large multiplicities of hadrons which are created. One can assume that the nuclear matter created in these collisions form an ideal gas that can be characterized by a grand-canonical ensemble. Using thermodynamic concepts to describe multi-particle production has a long history [55]. The concept of a temperature applies only to systems in at least local thermal equilibrium. The assumption of a locally thermalized source in chemical equilibrium can be tested by applying statistical thermal models to describe the ratios of various emitted particles.

The BRAHMS collaboration has reported results on particle ratios as a function of rapidity [56] as shown in Fig. 8 which depicts the rapidity dependence of the ratios $\bar{p}/p$, π^-/π^+ and K^-/K^+ produced in Au + Au collisions at the maximum RHIC energy, $\sqrt{s_{NN}}$ = 200 GeV. The ratios were obtained by integrating over both p_T and centrality. A strong rapidity dependence of the $\bar{p}/p$ ratio is evident, dropping from 0.75 ± 0.06 at the mid-rapidity region ($y = 0$) to 0.23 ± 0.03 at $y \simeq 3$. This is a large deviation from a boost invariant source where the ratios are constant; this indicates that as we move away from the low net-baryon central region, a baryon rich fragmentation region is reached. The π^-/π^+ ratio is consistent with unity (flat) over the considered rapidity range, while the K^-/K^+ ratio drops almost by 30% at y = 3 from its mid-rapidity value. The $\bar{p}/p$ and K^-/K^+ ratios are essentially constant in the rapidity interval $y = [0, 1]$.

As mentioned above, the measured set of particle ratios (or yields) at mid-rapidity lends itself to an analysis in terms of a model based on assuming the system is in chemical and thermal equilibrium. Figure 9 presents a recent comparison of the RHIC's experimental results and statistical thermal model calculations of hadron yields produced in Au + Au collisions at $\sqrt{s_{NN}}$ = 200 GeV [57]. The measurements were taken in the mid-rapidity region $|\eta| < 1$. They demonstrate quantitatively the high degree of equilibration achieved for hadron production in central Au+Au collisions at maximum RHIC energy. The numerical agreement between these calculations and the present measurements is excellent. The statistical thermal model reveals that the apparent species equilibrium was fixed at a temperature T_{ch} = 162 MeV and μ_B = 24 MeV. The ratios involving multi-strange baryons are well reproduced, as is the ϕ yield. Even the relatively wide resonances such as the K*'s fit well with the picture of a chemical freeze-out. The small value of the chemical potential, μ_B, indicates a small net baryon density at mid-rapidity at the RHIC which was confirmed by measurements of net-baryon rapidity distribution in Au + Au at $\sqrt{s_{NN}}$ = 200 GeV [58].

Figure 10 shows the STAR collaboration thermal model fit of temperature and baryon potential at chemical freeze-out as a function of collision centrality ($dN_{ch}/d\eta$) in collision systems Au + Au, Cu + Cu and $p+p$ [59]. The chemical freeze-out temperature, T_{ch}, is around 155 MeV and seemingly shows no dependence on the centrality and also no sensitivity to the colliding systems, yielding the same results for Au + Au and Cu + Cu data. The baryon chemical potential, μ_B, also showed no difference between the fits to Au + Au and Cu + Cu data. To study the validity of the statistical thermal fit considering a Grand Canonical formulation, the same fit was applied to the $p+p$ data. The chemical freeze-out temperature that results from this fit is slightly lower, $T_{ch} \simeq 150$ MeV [59].

This equilibrium population of species occurs both in elementary and nuclear collisions [60,61]. It was shown in

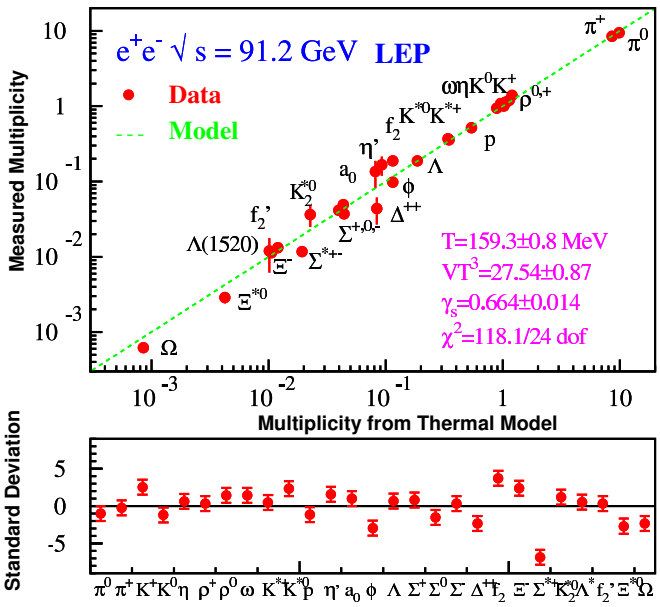

Fig. 11. Experimental hadron yields and statistical thermal model comparison for different particle species produced in LEP e^+e^- annihilation at $\sqrt{s}$ = 91.2 GeV. This figure is adapted from Ref. [62].

e^+e^- annihilation data at $\sqrt{s}$ = 91.2 GeV LEP energy, shown in the Fig. 11, are reproduced by the statistical hadronization model in its canonical form [62,63] and the derived temperature was T_{ch} = 165 MeV, in agreement with the limiting temperature predicted by Hagedorn [55] to occur in any multi-hadronic equilibrium system once the energy density approaches 0.6 GeV/fm^3. Thus, the upper limit of hadronic equilibrium density corresponds closely to the upper limit of energy density, ϵ_{crit} = 0.18 to 0.5 GeV/fm^3 of partonic equilibrium matter, according to lattice QCD [7,64]. This universal value of T_{ch} = 150 to 170 MeV is remarkably close to the critical temperature for the quark-hadron transition from Lattice QCD and it appears to be the universal hadronization temperature for e^+e^-, $p+p$ and heavy-ion collisions at high energy [62, 65]. To what extent this hints at the thermal behavior in e^+e^- and $p+p$ collisions is an important question, which is still under debate in our field. More recent data in d + Au and p + Pb as well in $p+p$ at RHIC and LHC energies provide new insight into the study of thermalization behavior in smaller systems compared to Au + Au and Pb + Pb.

2.3 QGP a nearly perfect fluid

The establishment of a new form of nuclear matter demands the observation of new collective properties distinct from previous measurements. The flow pattern of the thousands of particles produced in heavy-ion collisions is a key observable being adapted to search for new collective aspects [8,66,67,68,69]. The properties of collective flow examine two of the conditions required for satisfying the validity of the QGP hypothesis. The first is the degree of thermalization. Until now, no results are available from Lattice QCD regarding the non-equilibrium dynamics of a QGP. Nonetheless, the evolution of bulk matter from some initial conditions could be calculated through the equations of viscous relativistic hydrodynamics provided that local equilibrium is preserved. These equations can be approximated further by perfect fluid equations when the corrections due to viscosity could be neglected. This is conceivable when the scattering mean free paths are small compared to the scale of the spatial gradients of the fluid. The second condition is the validity of the numerically determined equation of state, i.e. the relationship between energy density and pressure. Under a specific initial boundary condition, the future evolvement of the matter then can be predicted [17]. To a good approximation, the data on elliptic flow confirms the idea that local thermal equilibrium is reached at RHIC energy and that the flow pattern is completely in agreement with numerical determinations of the equation of state from QCD.

However, collisions of two nuclei at relativistic energies create a partonic medium at extreme temperatures and densities, which will cool down by expansion and undergo a phase transition from a QGP back to hadronic matter. Studying collective behavior (like measurements of anisotropic particle flow) of strongly interacting matter in such conditions recently became one of the most active and fascinating topics in physics. The measurements of anisotropic particle flow and jet quenching at RHIC revealed a deconfined state of matter at high temperature and partonic density, that is characterized best as a near perfect fluid, i.e. a collective state with an extremely low ratio of shear viscosity to entropy density [10,11,12,13].

2.3.1 Anisotropic particle flow

The measurements of anisotropic particle flow, being connected to the collective behavior of the system, is an important observable in relativistic heavy-ion collisions as it signals the presence of multiple interactions between the constituents of the created matter. It was studied extensively in nucleus-nucleus collisions at the SPS and RHIC as a function of pseudorapidity, centrality, transverse momentum and energy [10,11,12,13,70,71,72,73]. The collective behavior of the constituents of created matter is explored by measuring the particles' azimuthal angular distributions with respect to the reaction plane. The direction of the reaction plane is defined by the impact parameter, b, of the colliding nuclei and the beam's direction, Fig. 12(a). In non-central collisions of heavy-ions at high energy, the configuration space anisotropy is converted into momentum space anisotropy, Figs.12(b)-(c). The method used to measure the particle flow is based upon the scheme described by Poskanzer and Voloshin [74] and, considering that nuclei have some density fluctuations [75,76], the strength of the n^{th} flow parameter is given by the n^{th} Fourier coefficient of the particle

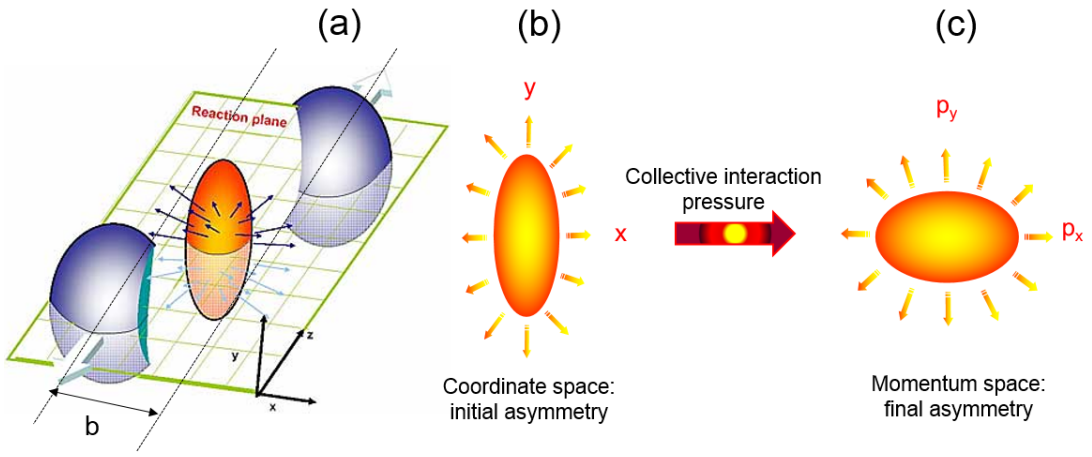

Fig. 12. Panel (a) presents schematically the collision zone between two incoming nuclei. Panel (b) illustrates initial-state anisotropy in the collision zone converting into final-state elliptic flow, and panel (c) measured as anisotropy in particle momentum.

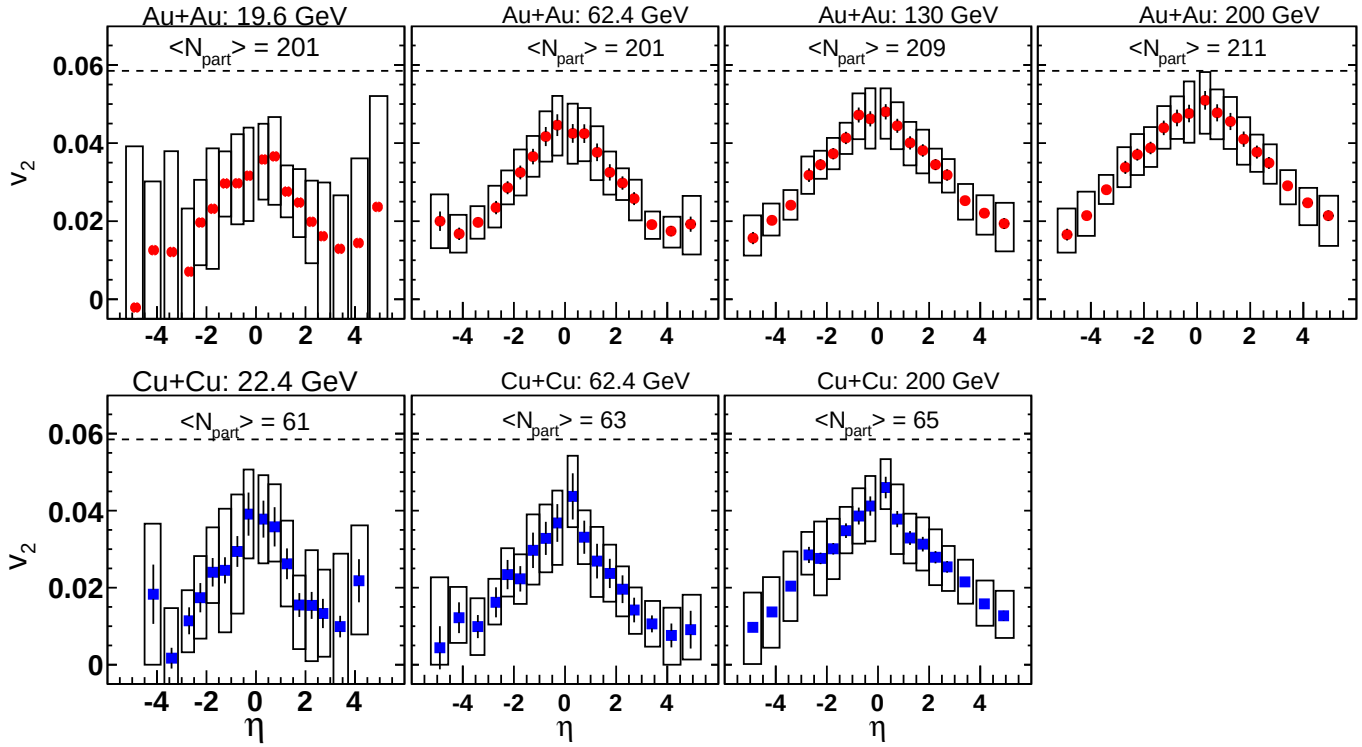

Fig. 13. The measured elliptic flow, v_2, vs η for Au + Au and Cu + Cu collisions at several RHIC energies.The boxes show the systematic errors and the bars represent the statistical errors [38,71,72,73].

azimuthal angle distribution described by the following equation:

$$\frac{dN}{d(\phi-\psi_n)} = \frac{1}{2\pi}\left(1+2\sum_{n=1}^{+\infty} v_n cos\ [n(\phi-\psi_n)]\right) \quad (2)$$

here ϕ is the azimuthal angle of each hadron. ψ_n is the n^{th} event plane, which varies due to event-by-event fluctuations [75,76]. ϕ and ψ_n are determined in the same reference frame (i.e. detector frame). The second Fourier expansion (quadrupole component), v_2, usually is defined as the strength of the elliptic flow.

The characterization of the collective flow of produced particles by their azimuthal anisotropy has proven to be one of the more fruitful probes of the dynamics in Au + Au collisions at RHIC. Elliptic flow, which is related to the initial spatial shape of the produced matter, has been of particular interest, as it can provide much information about

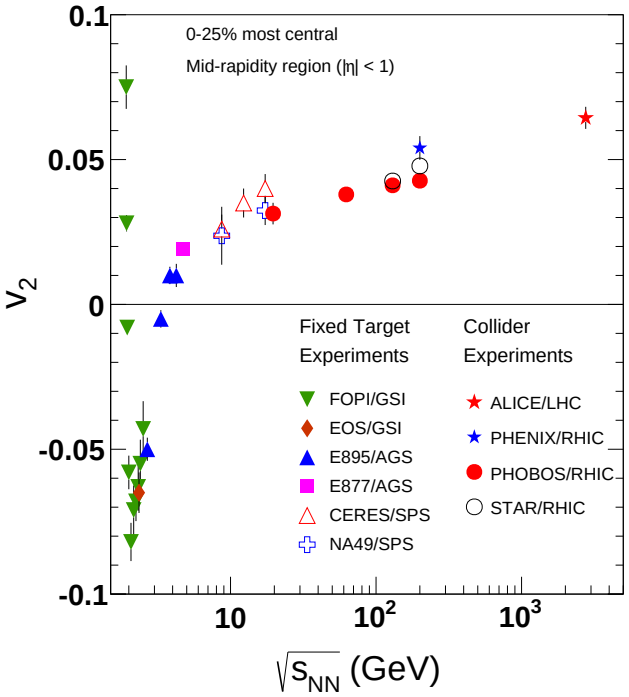

Fig. 14. Compilation of data using Refs. [79,80,81,82,83] of the dependence of integrated elliptic flow,v_2, on beam energy at GSI (Au + Au), AGS (Au + Au), SPS (Pb + Pb) and LHC (Pb + Pb).

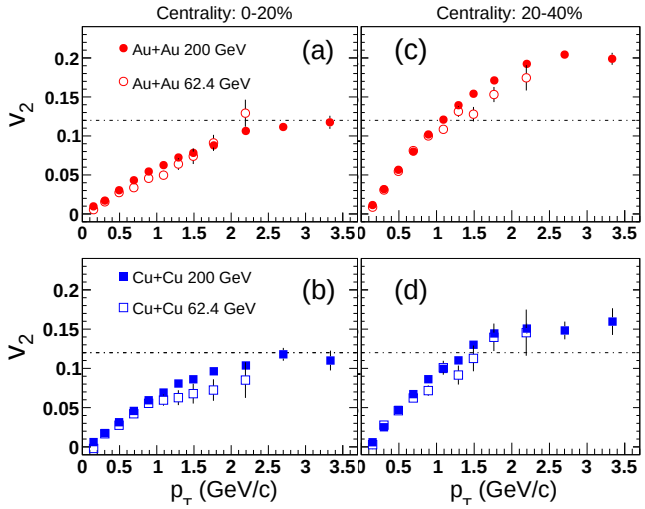

Fig. 15. The measured elliptic flow, v_2, vs p_T for Au + Au and Cu + Cu collisions at several RHIC energies for centrality bins 0-20% in panels (a)-(b) and 20-40% in panels (c)-(d). The boxes show the systematic errors and the bars represent the statistical errors [38,71,72,73].

the degree of thermalization of the hot, dense medium. Therefore, it is beneficial to study flow in multiple systems and compare. Specifically, Cu + Cu collisions are interesting as the copper nucleus is one-third of the size of gold. Exactly how flow scales between collision systems (e.g. a simple scaling with the system's size or geometry, the number of valence quarks, or transverse momentum) is crucial to understand the properties of the produced matter. The dependence of elliptic flow on the geometry, like Au + Au to Cu + Cu of the collision is of particular importance, as flow is thought to depend heavily on the initial spatial anisotropy. Additionally, any fluctuations would be expected to have more of an effect in a smaller system. The unique large pseudorapidity coverage of the PHOBOS detector ($|\eta| \leq 5.4$) made it ideally suited for probing the longitudinal structure of the collision, the dynamics of which have begun to be understood away from mid-rapidity [77].

Figure 13 shows the elliptic flow, v_2, signal as a function of pseudorapidity, η, in Au + Au collisions at $\sqrt{s_{NN}}$ = 19.6, 62.4, 130 and 200 GeV as well for Cu + Cu collisions at $\sqrt{s_{NN}}$ = 22.4, 62.4 and 200 GeV for the 0-40% most central events. The resemblance of Au + Au and Cu + Cu results is striking. The v_2 in the smaller system, Cu + Cu, collisions displays a similar shape in pseudorapidity and magnitude to that in Au + Au collisions at a given energy. The strength of the v_2 signal from Cu + Cu is surprising in light of expectations that the smaller size of the system would result in a much smaller flow signal [78].

For comparison, Fig.14 shows the dependence of the integrated elliptic flow of charged particles, v_2, on beam energy at GSI (EOS, FOPI experiments at CERN), AGS (E95 and E877 experiments at BNL), SPS (CERES and NA49 experiments at CERN), RHIC (PHENIX, PHOBOS and STAR experiments at BNL), and LHC (ALICE experiment at CERN) [79,80,81,82,83]. We observe that at low fixed target energies ($\sqrt{s_{NN}} \sim 3$ GeV), particle production is enhanced in the direction orthogonal to the reaction plane, and v_2 is negative. This is due to the effect that the spectator parts of the nuclei block the matter in the direction of the reaction plane. At higher center-of-mass energies, these spectator components move away sufficiently quickly, and therefore particle production is enhanced in the reaction plane, leading v_2 to be significantly different from zero. This phenomenon is expected in hydrodynamic scenarios in which the large pressure gradients within the reaction plane drive a stronger expansion. However, the important observation is that, up to the highest center of mass energies at RHIC, the observed asymmetry v_2 continues to grow. The ALICE measurement at 2.76 TeV shows that the integrated elliptic flow increases by about 30% compared to flow measured at the highest RHIC energy of 200 GeV. This result indicates that the hot and dense matter created in these collisions at the LHC energy (2.76 TeV) still behaves similar to matter created at RHIC [82,83].

Figure 15 presents the dependence of v_2 on the transverse momentum (p_T) of charged hadrons in Au + Au and Cu + Cu collisions at $\sqrt{s_{NN}}$ = 62.4 and 200 GeV for centrality bins 0-20% in panels (a)-(b) and 20-40% in panels (c)-(d). For both systems, the dependence of v_2 on p_T is similar to that for the two measured centrality classes, Au + Au and Cu + Cu. For a given system, the v_2 shows an increasing trend as a function of p_T, and there is a

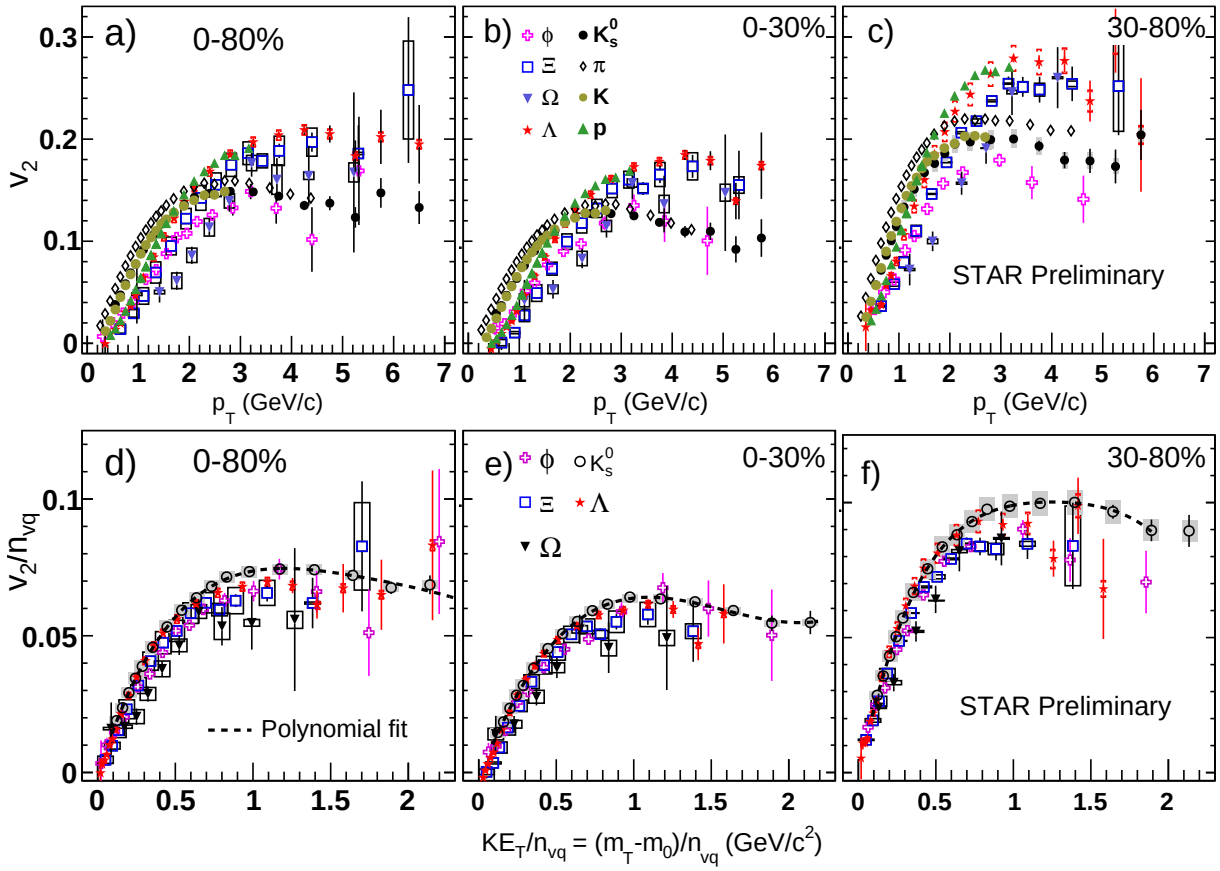

Fig. 16. Panels (a), (b) and (c): the identified hadron anisotropy, v_2, as a function of $p_{\rm T}$. Panels (d), (e) and (f): scaled identified hadron anisotropy, $v_2/{\rm n_{vq}}$ as a function of scaled transverse kinetic energy, ${\rm KE_T/n_{vq}}$. ${\rm n_{vq}}$ is the number of valence quarks in a given hadron (for mesons, ${\rm n_{vq}} = 2$; and, for baryons: 3). All data are from Au + Au collisions at $\sqrt{s_{NN}} = 200$ GeV. This figure is adapted from Ref. [84].

significant centrality dependence where the v_2 increases when moving from the most central collisions (0-20%) to mid-central ones (20-40%). This is consistent with what one would expect from the initial geometry of collisions because the most central collisions are more circular in shape, therefore a smaller v_2 is expected.

Figure 16(a)-(c) show the anisotropic flow distributions, v_2, of identified hadrons (ϕ, Ξ, Ω, Λ, K^0_S, π, K and p) as a function of the transverse momentum, $p_{\rm T}$. The results were measured for three collision centralities, 0-80%, 0-30% and 30-80% in Au + Au collisions at $\sqrt{s_{NN}}$ = 200 GeV [84]. In the lower $p_{\rm T}$ region, $p_{\rm T} \leq 2$ GeV/c, the value of v_2 is inversely related to the mass of the hadron, that is, characteristic of hydrodynamic collective motion in operation, Fig. 16(a)-(c). At the intermediate $p_{\rm T}$ region, the dependence is different. Instead of a mass dependence, there seems to be a hadron type dependence. We observed a splitting between baryon and meson v_2 at intermediate $p_{\rm T}$ for centrality 0-30%. However, for 30-80% centrality, no such distinct grouping was evident among the baryons and among the mesons.

An interesting result is that the multi-strange hadrons exhibit a smaller v_2 than other identified hadrons, i.e. the ϕ meson, whose mass is close to that of p and Λ, shows v_2 (ϕ) < $v_2(p)$. It is known that the ϕ meson does not participate as strongly as others do in hadronic interactions, nor can ϕ mesons be formed via the coalescence-like $K^+ + K^-$ process in high energy collisions [85]. Hence, the strong $v_2(\phi)$ we recorded must have developed before hadronization. This result offers evidence for partonic collectivity [86], which could also explain the reduce $v_2(\phi)$ in peripheral, as seen in Fig. 16(c).

To include the effect of the collective motion, usually the transverse momentum of the particle, $p_{\rm T}$, is transferred to the transverse kinetic energy ${\rm KE_T} \equiv {\rm m_T} - {\rm m_0} = \sqrt{p_{\rm T}^2 + {\rm m_0^2}} - {\rm m_0}$, where ${\rm m_0}$ is the particle's mass [84]. The measured v_2 was scaled by the number of valence quarks (NVQ) in a given hadron. For mesons and baryons, respectively, they are ${\rm n_{vq}} = 2$ and 3. The ${\rm KE_T}$ also was scaled with the same ${\rm n_{vq}}$. The results are shown in Fig. 16(d)-(f). The STAR collaboration observed for the first time the NVQ scaling in Au + Au at $\sqrt{s_{NN}}$ = 200 GeV for 0-80% collision centrality, it was considered as a good signature of partonic collectivity [87,88]. It is interesting to investigate the NVQ scaling for different centralities that

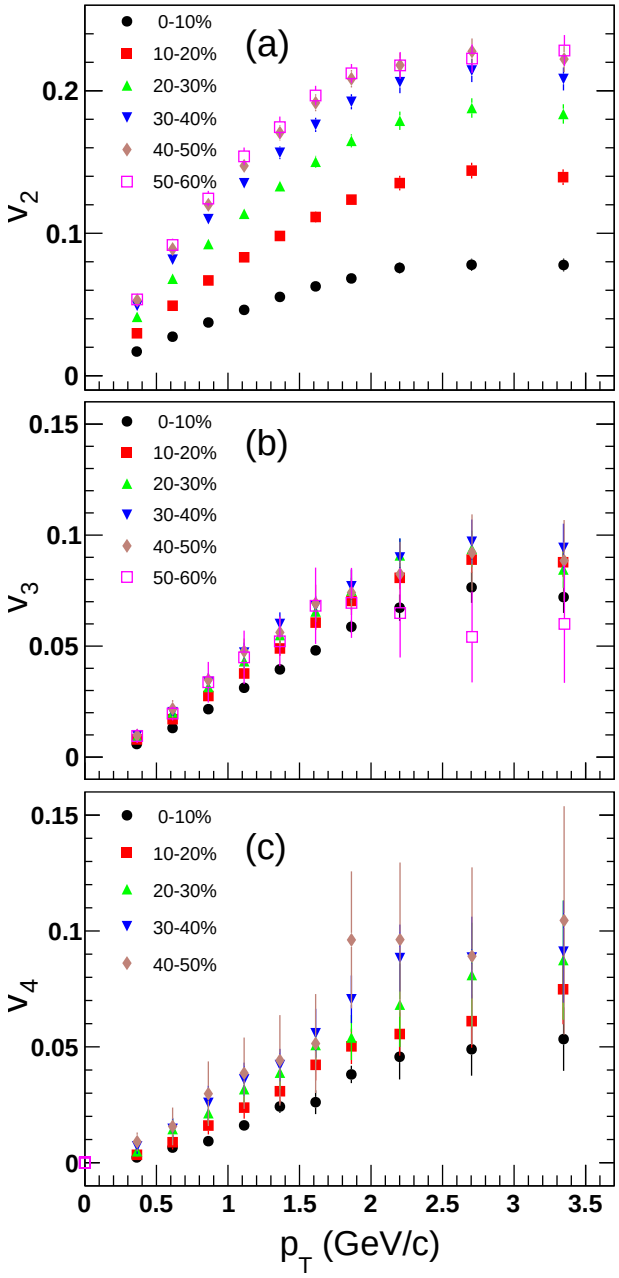

Fig. 17. The measured harmonic flow v_n (n = 2, 3 and 4) versus $p_{\rm T}$ measured in various centralities in Au + Au at $\sqrt{s_{NN}}$ = 200 GeV. Error bars show combined statistical and systematic errors. Figure is made using data from Ref. [90].

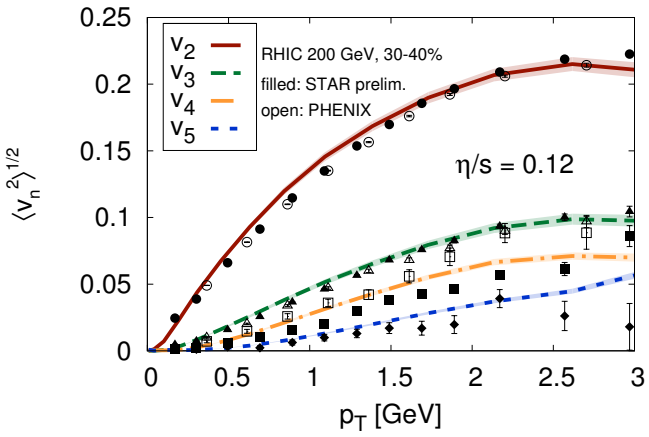

Fig. 18. The comparison of the RMS anisotropic flow coefficient, $\langle v_n^2(p_{\rm T})\rangle^2$, as a function of $p_{\rm T}$ measured in Au + Au at 200 GeV at RHIC to IP-Glasma model using constant shear viscosity to entropy density ratio, $\eta/s \approx 0.12$. This figure is adapted from Ref. [91].

could help us to understand partonic collectivity for different sized systems. Figure 16(d)-(f) shows v_2 scaled by n_{vq} as a function of KE_T/n_{vq} in Au + Au collisions at $\sqrt{s_{NN}}$ = 200 GeV for the same collision centralities discussed above. The results in Fig. 16(e) show that scaling holds for all identified strange hadrons for 0-30% centrality. This indicates that the major part of flow could be developed at the partonic phase for 0-30% centrality. On the other hand, for 30-80% centrality shown in the Fig. 16(f), the ϕ-meson deviates by about 10% from the fit line for the range $KE_T/n_{vq} > 0.6$ GeV/c. This could be interpreted as due to the small contribution from the partonic phase to collectivity. It should be noted that current LHC data, Pb + Pb collisions at $\sqrt{s_{NN}}$ = 2.76 TeV, exhibit deviations from the observed number of valence quark scaling at the level of about ± 20% for $p_{\rm T} > 3$ GeV/c [89].

Measuring the event's anisotropy components, v_n, is a powerful probe for investigating the characteristics of the created medium at RHIC. The results of the anisotropy of these higher-order events constrain the initial geometrical eccentricity and viscosity that are used in hydrodynamical models. The v_n of inclusive charged hadrons, where n = 2, 3, 4 and 5 are measured by RHIC experiments as a function of $p_{\rm T}$ in various centralities for Au + Au collisions at $\sqrt{s_{NN}}$ = 200 GeV [90], are shown in Figs. 17 and 18. All v_n exhibit an increasing trend as a function of $p_{\rm T}$ and v_2 is the dominant component. The third harmonic, or v_3, for which the main source is believed to be from fluctuation [75], shows an interesting behavior. Unlike v_2, the v_3 as a function of $p_{\rm T}$ is somewhat independent from collision centrality, which means the source of v_3 probably is not strongly influenced by the initial collision geometry. Also measurements of event-by-event v_3 provide additional constraints on theoretical models.

A good candidate for providing initial conditions for systematic flow studies is the Impact Parameter dependent Glasma (IP-Glasma) model described in detail in Refs. [91,92,93,94] and shown in Fig.18 as curves. It combines the IP-Sat (impact parameter saturation) model of high energy nucleon (and nuclear) wave functions with the classical SU(3) Yang-Mills dynamics of the Glasma fields produced in a heavy-ion collision. To describe the flow measurements, the IP-Glasma model of the classical early time evolution of boost-invariant configurations of gluon fields was coupled to a viscous hydrodynamic model to

describe the system's evolution [91]. Based on this comparison presented in Fig. 18, the data are well described by the IP-Glasma model given the systematic uncertainties in both the experimental and theoretical calculations [91]. The fact that the IP-Glasma model coupled with a viscous hydrodynamic model, which assumes the formation of a QGP, reproduces the experimental data implies that the fluctuations in the initial state are important and the created medium behaves as a nearly perfect liquid of nuclear matter because it has an extraordinarily low ratio of shear viscosity to entropy density, $\eta/s \approx 0.12$, see Fig.18. It even appears to be the most perfect fluid observed in nature so far, having a specific viscosity (viscosity to entropy density ratio) at least an order of magnitude smaller than that of any previously observed liquid.

3 Experimental evidence of created dense matter

3.1 High-$p_{\rm T}$ hadron suppression: jet-quenching

At high momentum, the perfect fluid collectivity is expected to breakdown, and in these models viscous corrections become large [95,96]. In Figs. 16, 17 and 18, instead of continuing to rise with $p_{\rm T}$, the elliptic asymmetry stops growing at $p_{\rm T} > 2$ GeV/c, and the difference between baryon versus meson, v_2 became distinct as in Fig. 16(b). In a coalescence picture, the quarks contributing to baryons are at lower momentum and so more strongly coupled compared to these for meson [97]. Furthermore, the PHENIX collaboration reported an important result at RHIC is that the non-equilibrium power-law high-$p_{\rm T}$ particle distributions persist, but are strongly quenched [98,99]. Figure 19 compares the π^0 invariant differential cross sections obtained from minimum-bias $p+p$ collisions at 200 GeV to Au + Au collisions at the same energy and for two collision centralities: (a) 0-10%, and, (b) 80-92% [98,99]. For comparison, the $p+p$ data are scaled by $N_{\rm coll}$, corresponding to the centrality in Au + Au collisions. The scaled $p+p$ data are well parameterized by a power-law form $A(1\ p_{\rm T}\ /p_0)^{-n}$, with parameters of $A =$ 393 mb GeV^{-1} c^3, $p_0 = 1.2112$ GeV/c, and $n = 9.97$ as in [98,99]. We also observe that the scaled $p+p$ data are well reproduced by the NLO pQCD calculations [98, 99]. Figure 19(a) shows clearly that the π^0 invariant yield from central (0-10%) Au + Au collisions as a function of $p_{\rm T}$ are suppressed compared to the π^0 invariant yield from $p+p$ collisions at the same $p_{\rm T}$. This is clear experimental evidence of the quenching phenomena of π^0 in central Au + Au collisions at maximum RHIC energy, $\sqrt{s_{NN}} =$ 200 GeV. In contrast, for the Au + Au peripheral collisions (80-92%) shown in Fig. 19(b), the production rate of π^0 particles agrees well with π^0 particles production in $p+p$ collisions and in the pQCD theoretical predictions.

We quantify the medium effects on high $p_{\rm T}$ production in nucleus-nucleus collisions, A + A, with the nuclear

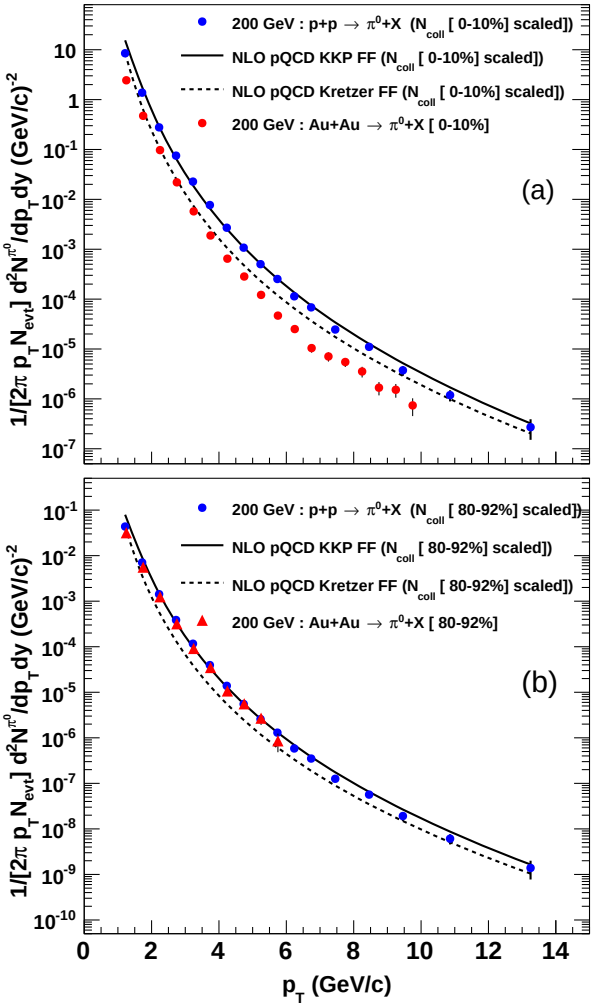
200 GeV : p+p → π⁰+X (N_coll [0-10%] scaled])
NLO pQCD KKP FF (N_coll [0-10%] scaled])
NLO pQCD Kretzer FF (N_coll [0-10%] scaled])
200 GeV : Au+Au → π⁰+X [0-10%]
(a)
200 GeV : p+p → π⁰+X (N_coll [80-92%] scaled])
NLO pQCD KKP FF (N_coll [80-92%] scaled])
NLO pQCD Kretzer FF (N_coll [80-92%] scaled])
200 GeV : Au+Au → π⁰+X [80-92%]
(b)
1/[2π p_T N_evt] d²N^π⁰/dp_T dy (GeV/c)^-2
p_T (GeV/c)

Fig. 19. Invariant differential cross section for inclusive π^0 production (points) and the results from NLO pQCD calculations with the same scaling using the Kniehl-Kramer-Potter (solid line) and Kretzer (dashed line) sets of fragmentation functions. The $p+p$ data are scaled by the number of binary collisions, $N_{\rm coll}$, corresponding to the centrality class in Au + Au collisions: panel (a) 0-10% and panel (b) 80-92%. Data used in the figure were taken from Refs. [98,99].

modification factor which is defined as follows:

$$\mathrm{R_{AA}(p_T)} = \frac{1}{\langle \mathrm{N_{coll}} \rangle} \times \frac{\text{yield per A + A collision}}{\text{yield per } p+p \text{ collision}}$$

$$= \frac{1}{\langle \mathrm{N_{coll}} \rangle} \times \frac{\mathrm{d^2N^{A+A}/d\eta dp_T}}{\mathrm{d^2N^{p+p}/d\eta dp_T}}$$

This factor reflects the deviation of measured distributions of nucleus-nucleus, A + A, transverse momentum, at given impact parameter b, from measured distributions of an incoherent superposition of nucleon-nucleon ($p+p$) transverse momentum ($\mathrm{R_{AA}} = 1$). This normalization often is known as "binary collisions scaling". In the absence of any modifications due to the 'embedding' of elementary

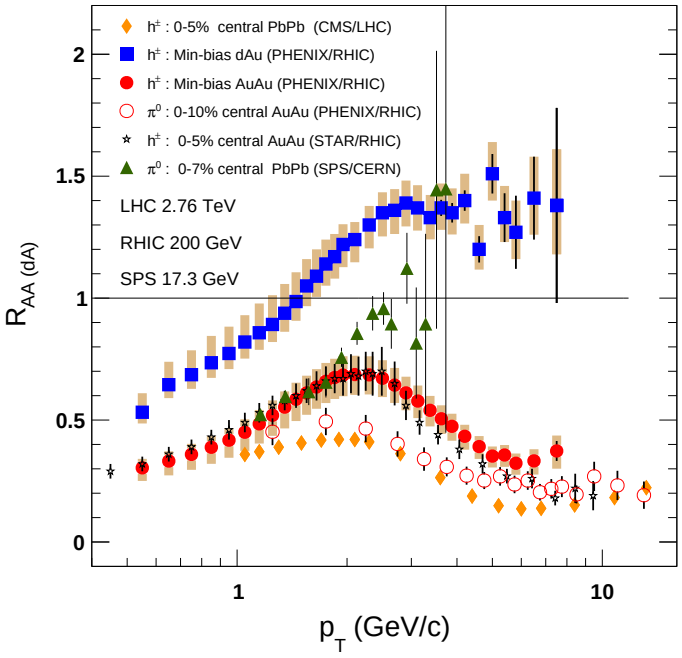
h± : 0-5% central PbPb (CMS/LHC)
h± : Min-bias dAu (PHENIX/RHIC)
h± : Min-bias AuAu (PHENIX/RHIC)
π0 : 0-10% central AuAu (PHENIX/RHIC)
h± : 0-5% central AuAu (STAR/RHIC)
π0 : 0-7% central PbPb (SPS/CERN)
LHC 2.76 TeV
RHIC 200 GeV
SPS 17.3 GeV
R_AA (dA)
p_T (GeV/c)

Fig. 20. The evolution of the nuclear modification factor with center-of-mass energy, from the SPS [100] to RHIC [38,103,104,105,106,107,108] and then to the LHC [109]. The error bars correspond to the statistical errors. For clarity, the systematic errors are shown as vertical bands.

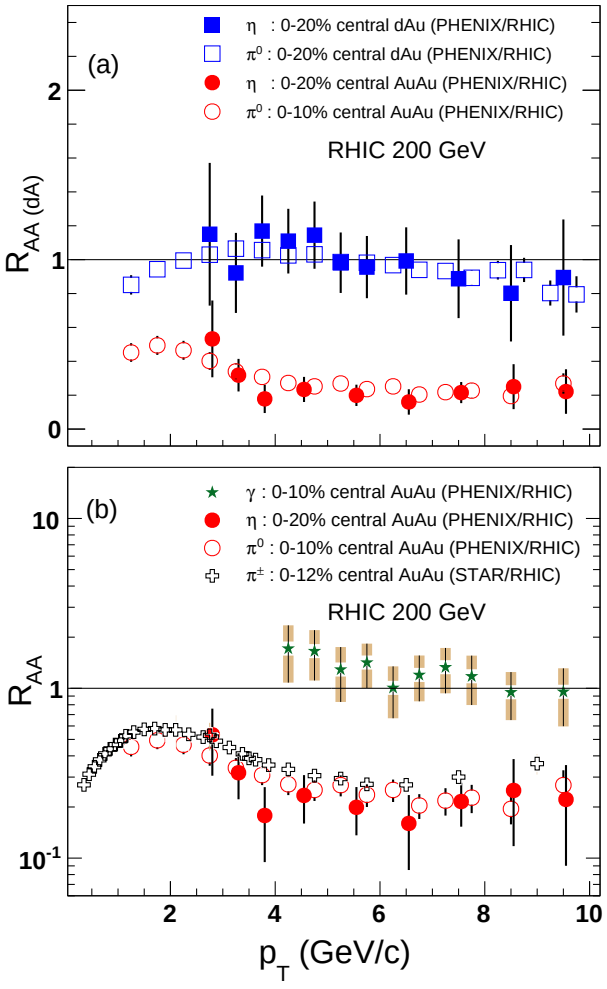
(a)
η : 0-20% central dAu (PHENIX/RHIC)
π0 : 0-20% central dAu (PHENIX/RHIC)
η : 0-20% central AuAu (PHENIX/RHIC)
π0 : 0-10% central AuAu (PHENIX/RHIC)
RHIC 200 GeV
R_AA (dA)
(b)
γ : 0-10% central AuAu (PHENIX/RHIC)
η : 0-20% central AuAu (PHENIX/RHIC)
π0 : 0-10% central AuAu (PHENIX/RHIC)
π± : 0-12% central AuAu (STAR/RHIC)
RHIC 200 GeV
R_AA
p_T (GeV/c)

Fig. 21. The nuclear modification factor R_{AA} from $Au+Au$ collisions and R_{dA} of $d+Au$ collisions at $\sqrt{s_{NN}}$ = 200 GeV using Refs. [38,103,104,105,106,107,108]. Panel (a) compares R_{AA} with R_{dA} for π^0 and η from central $Au+Au$ and $d+Au$ collisions. Panel (b) compares the R_{AA} of Direct γ with R_{AA} of π^0, η and $\pi^{\pm}$ in central $Au+Au$ collisions. The error bars correspond to the statistical errors. For clarity, the systematic errors are shown as vertical bands.

collisions in a nuclear collision, we expect $R_{AA}=1$ at high-p_T. At low p_T, where particle production follows a scaling with the number of participants, the above definition of R_{AA} leads to $R_{AA}<1$ for $p_T<2$ GeV/c.

At maximum SPS energy ($Pb+Pb$ $\sqrt{s_{NN}}=17.3$ GeV), the WA98 data for $R_{AA}(p_T)$ presents an enhancement of moderately high-p_T tails in central $Pb+Pb$ collisions [100]. This enhancement was anticipated as a result of the Cronin effect [101]. Another experimental observation in heavy-ion collisions (from AGS to RHIC energies) is that hadron production at mid-rapidity ($|y|<1.5$) rises logarithmically with increasing collision energy. At RHIC, the central zone is approximately net-baryon-free [102]. Particle production is large and dominated by pair production, and the energy density seems to exceed significantly that required for QGP formation [10,11,12,13].

The evolution of the nuclear modification factor with center-of-mass energy, from the SPS [100] to RHIC [38,103,104,105,106,107,108] and then to the LHC [109], is presented in Fig. 20. We observe that in the presented p_T region, charged hadron production at the LHC is found to be about 50% more suppressed than at RHIC, and has a similar suppression value as for neutral pions (π^0) measured by PHENIX. These measurements of $R_{AA}(p_T)$ at RHIC and LHC is consistent with a large energy loss in the medium causing it to become opaque to the propagation of high momentum partons. In contrast, $R_{AA}(p_T)$ for π^0 at SPS energy, as shown Fig. 20, exhibit enhancement similar to the $d+Au$ at RHIC.

RHIC experiments, as shown Fig. 20, revealed the suppression of the high-p_T hadron spectra at the mid-rapidity region in central $Au+Au$ collisions compared to the scaled momentum spectra from $p+p$ collisions at the same energy, $\sqrt{s_{NN}}=200$ GeV. This effect, proposed by Bjorken, Gyulassy, and others [110,111] rests on the expectation of a large energy loss of high momentum partons scattered in the initial stages of collisions in a medium with a high density of free color charges. According to the QCD theory, colored objects will lose energy via bremsstrahlung radiation of gluons [112]. Such a mechanism strongly would degrade the energy of leading partons, as reflected in the reduced transverse momentum of leading particles in the jets emerging after their fragmentation into hadrons. This energy loss is expected to depend strongly on the color

charge density of the created system, and the path length traversed by the propagating parton. It has been recognized that the elastic energy loss is too small to engender significant attenuation of the jet in the created medium [113]. The STAR experiment at RHIC established that the topology of high-p_T hadron's emission is consistent with jet emission, so that jet-suppression is a valid concept and is elaborated in the next section.

In $d+\mathrm{Au}$ collisions at $\sqrt{s_{NN}} = 200$ GeV, see Fig. 20, the R_{dA} for charged hadrons $(h^+ + h^-)/2$ is enhanced. This enhancement is an initial state effect [114] known by Cronin effect which also is seen in $p+\mathrm{A}$ collisions. The Cronin effect is associated with the initial multiple scattering of high momentum partons. In contrast, the RHIC results show a factor of 4 to 5 suppression in central $\mathrm{Au}+\mathrm{Au}$ (at $\sqrt{s_{NN}} = 200$ GeV). In the same context, the R_{dAu} of π^0 and η in central $d+\mathrm{Au}$ collisions exhibited no suppression of high-p_T, in contrast with the R_{AA} of π^0 and η in central $\mathrm{Au}+\mathrm{Au}$ collisions that is suppressed, as shown in Fig. 21(a). At $p_T \sim 4$ GeV/c, we find a ratio $R_{dAu}/R_{AA} \approx 5$. Indeed, the R_{dA} distribution shows the Cronin type enhancement observed at lower energies as in $\mathrm{Pb}+\mathrm{Pb}$ collisions at 17.3 GeV/c [17,100] as shown in Fig. 20.

Figure 21(b) summarizes the R_{AA} for direct photons, π^0 and η in central $\mathrm{Au}+\mathrm{Au}$ collisions at $\sqrt{s_{NN}} = 200$ GeV. The R_{AA} for direct photons are not suppressed as they do not interact strongly with the medium. The R_{AA} for both π^0, $\pi^{\pm}$ and η's mesons exhibit the same suppression relative to the point-like scaled $p+p$ data by a factor of ~ 5 that appears to be constant for $p_T > 4$ GeV/c while the η mass is much larger than that of π^0 (and $\pi^{\pm}$). These observations of high-p_T hadron suppression, combined with the collectivity results from Fig. 16, suggest that the QCD medium created at RHIC is both partonic and opaque. Adding to this discovery of suppression of particles at high transverse momentum, two very striking results were seen for open heavy flavor from the PHENIX experiment via the measurement of electrons from the semi-leptonic decays of hadrons carrying charm or bottom quarks [103,104,105,106]. First, heavy mesons, despite their large mass, exhibit a suppression at high transverse momentum compared to that expected from $p+p$ collisions [104,115,116]. This suppression is similar to that of light mesons, which implies a substantial energy loss of fast heavy quarks while traversing the medium, see Fig. 22(a). Second, an elliptic flow is observed for heavy mesons, electrons from semi-leptonic decays of hadrons carrying charm or bottom quarks, that is comparable to that of light mesons like pions, Fig. 22(b). This implies that the heavy quarks in fact are sensitive to the pressure gradients driving hydrodynamic flow giving new insights into the strongly coupled nature of the QGP fluid at these temperatures.

These data on heavy mesons R_{AA} were described by theoretical calculations of the parton energy loss in the matter created in Au+Au collisions as shown in the Fig. 22 [108,117,118]. From these theoretical frameworks, we learned that the gluon density dN_g/dy must be approximately

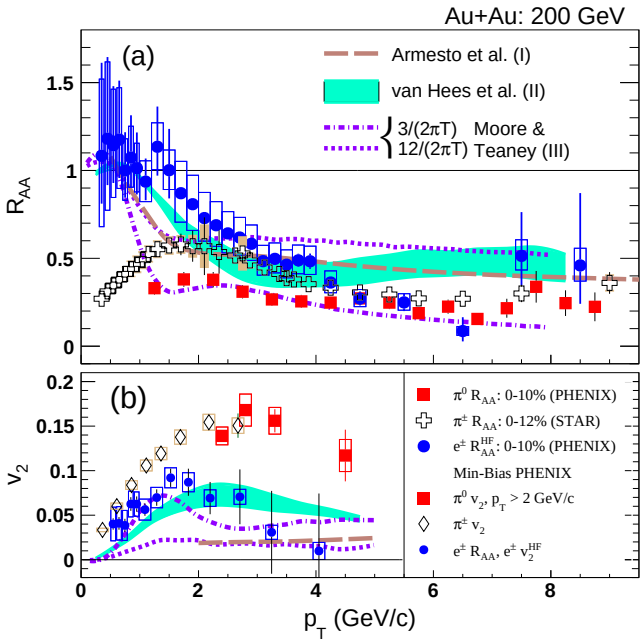

Fig. 22. The nuclear modification factor, R_{AA}^{HF}, for HF electrons compared with the R_{AA} of π^0 in central Au+Au collisions at $\sqrt{s_{NN}} = 200$ GeV, see panel (a). Panel (b) considers the anisotropic flow of HF electrons v_2^{HF} with that of v_2 of π^0 and $\pi^{\pm}$ in minimum-bias Au+Au collisions [38,104,107,108,115,116].

1000, and the energy density of the matter created in the most central collisions must be approximately 15 GeV/fm^3 to account for the large suppression observed in the data [119,120].

3.2 Dijet fragment azimuthal correlations: opaque medium

Hard-scattering processes were established at high-p_T in elementary collisions at high energy through the measurement of jets [121,122,123], back-to-back jets (dijets) [124], high-p_T single particles, and back-to-back correlations between high-p_T hadrons [125]. Jets were shown to carry the momentum of the parent parton [126]. The jet's cross sections and high-p_T single particle spectra are well described over a broad range of energies in terms of the hadrons parton distributions, hard parton scattering treated by pQCD, and subsequent fragmentation of the parton [127,128,129]. In the absence of the effects of the nuclear medium, the rate of hard processes should scale linearly with the number of binary nucleon-nucleon collisions.

Results from RHIC, described above, show a suppression of the single particle's inclusive spectra of hadrons for $p_T > 2$ GeV/c in central $\mathrm{Au}+\mathrm{Au}$ collisions, indicating substantial in-medium interactions [130,131]. The study of high transverse momentum hadron production in heavy-ion collisions at RHIC provides the opportunity to probe in more detail the evolution of the matter produced and

experimentally probe the QCD matter in the most dense stage of the collisions, wherein quark-gluon deconfinement is likely to occur [132]. Measurements of two-hadron angular correlations, as seen in Fig. 23, at large transverse momentum for $p+p$ and Au + Au as well as $d+$Au collisions at the same energy, $\sqrt{s_{NN}} = 200$ GeV, provide evidence for the production of jets in high-energy nucleus-nucleus collisions and allow first measurements, inaccessible in inclusive spectra, of the fate of back-to-back jets in the dense medium, thereby serving as a tomography probe of the medium.

The STAR collaboration established the first measurements of two-particle azimuthal distribution $D(\Delta\phi)$, defined as

$$D(\Delta\phi) = \frac{1}{N_{trigger}} \frac{1}{\epsilon} \frac{dN}{d(\Delta\phi)} \qquad (3)$$

at the mid-rapidity region $|\eta| < 0.7$. $N_{trigger}$ is the number of particles defined in specific $p_{\rm T}$ range, referred to as trigger particles. ϵ is the tracking efficiency of the associated particles [133,134,135].

Figure 23 shows the discovery of mono-jet production [136] in central Au + Au collisions at the maximum RHIC energy. The pedestal-subtracted azimuthal distributions for high-$p_{\rm T}$ pairs in $p+p$ and central $d+$Au collisions show clear di-jet features. The azimuthal distributions are shown also for central Au + Au collisions after subtracting the elliptic flow and pedestal contributions [133]. The measurements were obtained with a trigger particle $\rm p_T^t$ under the condition $4 < \rm p_T^t < 6$ GeV/c, along with an associated particle with $\rm p_T^a$: 1) for $2 < \rm p_T^a < p_T^t$ GeV/c as shown in Fig. 23(a), and 2) for $0.15 < \rm p_T^a < 4$ GeV/c as shown in Fig. 23(b). The two-particle correlation is presented as a function of the difference between the azimuthal angles of the two particles ($\Delta\phi$) produced in the Au + Au, $d+$Au and $p+p$ collisions at the same energy, $\sqrt{s_{NN}} = 200$ GeV.

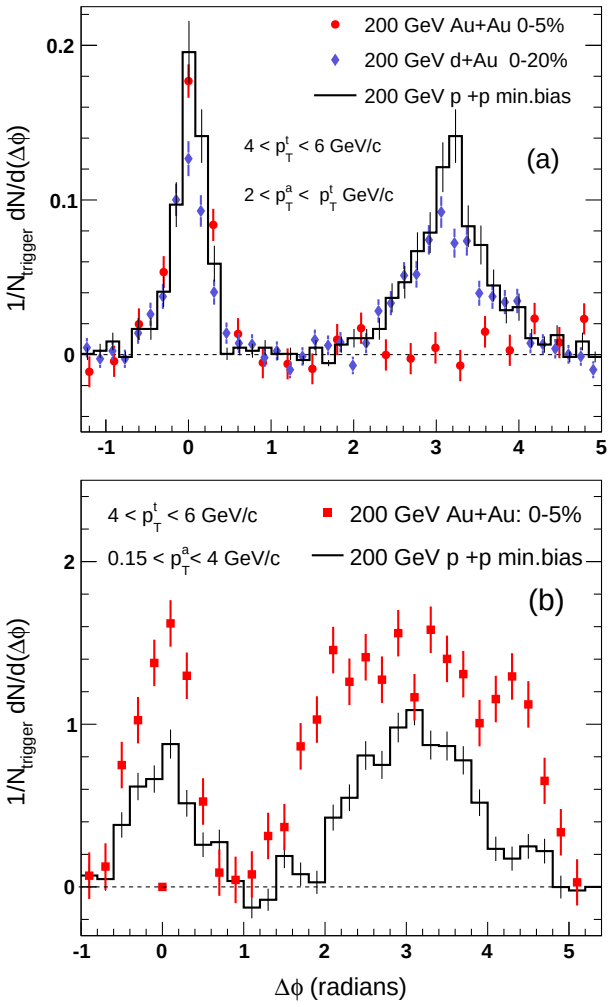
200 GeV Au+Au 0-5%
200 GeV d+Au 0-20%
200 GeV p +p min.bias
4 < p_T^t < 6 GeV/c
2 < p_T^a < p_T^t GeV/c
(a)
1/N_trigger dN/d(Δφ)
4 < p_T^t < 6 GeV/c
0.15 < p_T^a < 4 GeV/c
200 GeV Au+Au: 0-5%
200 GeV p +p min.bias
(b)
Δφ (radians)

Fig. 23. The two-particle angular correlations measurements in Au + Au, $d+$Au and $p+p$ collisions at $\sqrt{s_{NN}} = 200$ GeV in the presence of a trigger particle with $\rm p_T^t$ under the condition $4 < \rm p_T^t < 6$ GeV/c, and an associated particle with $\rm p_T^a$: panel (a) for $2 < \rm p_T^a < p_T^t$ GeV/c, and panel (b) for $0.15 < \rm p_T^a < 4$ GeV/c. The non-correlated background and the flow background were subtracted [38,134,135].

The results illustrated in Fig. 23(a) demonstrate that the trigger-side correlation peak (at $\Delta\phi = 0$) in central Au + Au collisions apparently is the same as that measured in $p+p$ and $d+$Au collisions but the away-side jet correlation (at $\Delta\phi = \pi$) in Au + Au has vanished. This observation is consistent with a large energy loss in the medium causing it to become opaque to the propagation of high momentum partons. However, it is noticeable in Fig. 23(b), which has a wide $\rm p_T^a$, $0.15 < \rm p_T^a < 4$ GeV/c, that the jets on the away side have not disappeared, but simply lost energy so that the away-side correlation peak has become much wider than that of the $p+p$ collisions. These collective measurements, from $p+p$, $d+$Au and Au + Au of two-particle correlations, point to the creation of a dense medium in central Au + Au collisions at $\sqrt{s_{NN}} = 200$ GeV.

The main goal was to measure the dijet fragment azimuthal correlations in $d+$Au collisions at similar energy as in Au + Au collisions, so as to check the interpretation of high-$p_{\rm T}$ suppression in Au + Au at $\sqrt{s_{NN}} = 200$ GeV; quenching was due to initial state saturation (shadowing) of the gluon distributions and/or to jet quenching at the final state. One method to asset the QGP final state interactions was by substituting a deuterium beam for one of the two heavy nuclei of Au + Au and it has been predicted that such a control test would be essential to set apart the unknown nuclear gluon shadowing contribution to the A+A quench pattern [137]. Furthermore, $d+$Au was proposed to test the predictions of the possible initial state Cronin multiple interactions [114,138,139,140]. In contrast, one model of the Color Glass Condensate anticipated a substantial suppression in $d+$Au collisions at $\sqrt{s_{NN}} = 200$ GeV [141]. The RHIC results [142,143,144,145] definitively rule out a large initial shadowing as the cause of the quenching in Au + Au (shown in Figs. 20 and 21). The return of back-to-back jet correlation in $d+$Au to the level observed in $p+p$ is illustrated in Fig. 23(a). The results turn out consis-

tent with jet quenching as a final state effect in Au + Au. These d + Au results hold the conclusion that the observed jet quenching in Au + Au is due to the partons' energy loss [118]. Jet quenching theoretical analyses support the estimates of energy density determined from measuring charged particle multiplicity by RHIC experiments. They estimated large energy losses for jets propagating through the medium, and enhance the case for multiple strong interactions of the QGP constituents of the medium created at RHIC [146].

4 Conclusions

Quantum chromodynamics, QCD, is the base of the Standard Model, providing a fundamental description of hadron physics in terms of quark and gluon degrees of freedom. The theory has been checked broadly, particularly in inclusive and exclusive processes including collisions at large momentum transfer where factorization theorems and the smallness of the QCD effective coupling concede perturbative predictions [147]. QCD is a very rich and complex theory, prominent to many new physical phenomena. Ultrarelativistic heavy-ion collisions offer the unique ability to investigate hot and dense QCD matter under laboratory conditions. However, due to the fundamental confining properties of the physical QCD vacuum, the deconfined quanta (i.e. the quarks and gluons) are not directly observable. What is observable are hadronic and leptonic residues of this transient deconfined state. Collisions of protons or heavy-ions, which are accelerated to nearly the speed of light, are an excellent system to study these interactions in more detail. In contrast to proton-proton collisions, where only a small number of particles are created, the particle production in heavy-ion collisions is so enormous that a QCD medium with collective behavior and unique properties is produced. It consists of quarks and gluons and is, therefore, called the quark gluon plasma, QGP. Relativistic heavy-ion collisions are carried out, for instance, at the LHC at CERN and RHIC at BNL, where experimental evidence was found that in those collisions a new state of nuclear matter indeed is produced.

In this review article, we have focused on measurements as a function of system sizes, collision centrality and energy carried out in RHIC experiments. We have presented experimental measurements on the production of bulk particles, the initial conditions of the collisions, the particle ratios and the chemical freeze-out conditions for different particle species, as well as the flow anisotropy of particles, high-p_t hadron suppression, dijet fragment azimuthal correlations, and heavy flavors probes. We compared these experimental measurements to theoretical model calculations. The measurements suggest that RHIC discovered a new state of matter in central Au + Au collisions at $\sqrt{s_{NN}} = 200$ GeV. This new form of matter is hot, dense, and strongly interacting, and is consistent with the hot, dense state as predicted from QCD. Precision measurements already are providing detailed information on its initial conditions and transport properties. Whilst this material, and its discovery, is far from being fully understood, the focus of the RHIC experiments, for instance, is on a detailed exploration of the properties of this new state of nuclear matter, QGP, by upgrading the detectors and beam luminosities.

In 2010, the LHC entered the field of relativistic heavy-ion physics with a very impressive performance. With a wealth of results within a few months after the first collisions, the LHC heavy-ion program has benefited from many years of preparation, a very strong and complementary set of detectors, and a decade of experience and progress made at RHIC. The number of new observations into the properties of QCD matter under extreme conditions continues to rise. The conclusion established at RHIC, that a hot, dense medium that flows with a viscosity-to-entropy density ratio close to the conjectured lower bound and quenches the energy of hard probes was confirmed at the LHC. However, one cannot avoid pointing out that recent experimental results from LHC and RHIC provide new insight into the role of initial and final state effects both in p + Pb and d + Au collisions. The latter have proven to be interesting and more surprising than original anticipated; and could conceivably shed new light in our understanding of collective behavior in heavy-ion physics. Therefore, the experiments at RHIC and the LHC are probing complementary kinematic regions and main goal of the present project is to attain, at both colliders, an understanding of the properties of the matter created, QGP, that is believed to be the primordial matter present in the Early Universe

Acknowledgements

The author thanks F. Karsch, B. Schenke, P. Stankus, C. Beck, D. Morrison, M. McCumber and L. McLerran for their stimulating discussions. P. Tribedy, R. Venugopalan and A. Andronic are warmly thanked for useful suggestions and for providing model calculations plotted on Figs. 5 and 9. C. Roy and Institut Pluridisciplinaire Hubert Curien (IPHC) as well as A. Nourreddine and Université de Strasbourg are fully acknowledge for their supports for HDR ("Habilitation à Diriger des Recherches") where parts of the present review paper were presented in the HDR written document available at:
https://tel.archives-ouvertes.fr/tel-00925262.
The author's research was supported by US Department of Energy, DE-AC02-98CH10886.

References

1. E. Shuryak, Phys. Rep. **61**, 71 (1980).
2. L. McLerran, Rev. Mod. Phys. **58**, 1021 (1986).
3. M. Hindmarsh and O. Philipsen Phys. Rev. D **71**, 08730 (2005).
4. http://www.jicfus.jp/en/promotion/pr/mj/guido-cossu/
5. S. Borsanyi, G. Endrodi, Z. Fodor, A. Jakovac, S, D. Katz, S. Krieg, C. Ratti, K. K. Szabo, Journal of High Energy Physics, **11**, 077 (2010).

6. S. Borsanyi, Z. Fodor, C. Hoelbling, S. D. Katz, S. Krieg, K. K. Szabo, Phys. Lett. B **370**, 99 (2014).
7. A. Bazavov A. Bazavov, T. Bhattacharya, C. DeTar, H. Ding, S. Gottlieb, R. Gupta, P. Hegde, U.M. Heller, F. Karsch, E. Laermann *et al.*, Phys. Rev. D **90**, 094503 (2014).
8. H. G. Baumgardt, J. U. Schott, Y. Sakamoto, E. Schopper, H. Stöcker, J. Hofmann, W. Scheid and W. Greiner, Z. Phys. A **273**, 359 (1975).
9. J.D. Bjorken, Phys. Rev. D **27**, 140 (1983).
10. I. Arsene *et al.* (PHENIX Collaboration), Nucl. Phys. A **757**, 1 (2005).
11. B. B. Back *et al.* (PHOBOS Collaboration), Nucl. Phys. A **757**, 28 (2005).
12. J. Adams *et al.* (BRAHMS Collaboration), Nucl. Phys. A **757**, 102 (2005).
13. K. Adcox *et al.* (STAR Collaboration), Nucl. Phys. A **757**, 184 (2005).
14. M. Harrison, T. Ludlam, S. Ozaki, Nuclear Instruments and Methods in Physics Research A **499**, 235 (2003).
15. http://www.agsrhichome.bnl.gov/RHIC/Runs/
16. I. Alekseev, C. Allgower, M. Bai, Y. Batygin, L. Bozano, K. Brown, G. Bunce, P. Cameron, E. Courant, S. Erin *et al.*, Series: C-A/AP - Report Number: C-A/AP/455; BNL-97226-2006-IR.
17. M. Gyulassy and L. McLerran, Nucl. Phys. A **750**, 30 (2005).
18. G. Aad *et al.* (ATLAS Collaboration), Phys. Rev. Lett. **114**, 072302 (2015).
19. K. Aamodt *et al.* (ALICE Collaboration), Phys. Lett. B **734**, 31 (2014).
20. V. Khachatryan *et al.* (CMS Collaboration), Journal of High Energy Physics, **09**, 091 (2010).
21. G. Aad *et al.* (ATLAS Collaboration), Phys. Rev. Lett. , **110**, 182302, (2013).
22. B. Abelev *et al.* (ALICE Collaboration), Phys. Lett. B **726**, 164 (2013).
23. L. Milano (ALICE Collaboration), J. Phys. Conf. Ser. **509**, 012105 (2014).
24. A. Adare *et al.* (PHENIX Collaboration), Phys. Rev. Lett. **98** 232301 (2007).
25. X. Zhao and R. Rapp, Phys. Lett. B **664**, 253 (2008).
26. Y. Liu, Q. Zhen, N. Xu and P. Zhuang, Phys. Lett. B **678**, 72 (2009).
27. R. Vogt, Phys. Rev. C **71**, 054902 (2005).
28. D. Kharzeev, C. Lourenco, M. Nardi, and H. Satz, Z. Phys. C **74**, 307 (1997).
29. K. J. Eskola, H. Paukkunen, and C. A. Salgado, JHEP **04**, 065 (2009).
30. J. L. Nagle, A. D. Frawley, L. A. Linden Levy, and M. G. Wysocki, Phys. Rev. C **84**, 044911 (2011).
31. R. Nouicer *et al.* (PHOBOS Collaboration), Eur. Phys. J. C **33**, S606 (2004).
32. S. Ahmad, A. Ahmad, A. Chandra, M. Zafar and M. Irfan, Advances in High Energy Physics, **2013**, 836071 (2013).
33. R. Nouicer *et al.* (PHOBOS Collaboration), published in 2002 QCD and Hadronic Interactions, edited by Tran Thanh Van (The Gioi Publishers, Hanoi, 2002), pp. 381.
34. R. J. Glauber, G. Matthiae, Nucl. Phys. B **21**, 135 (1970).
35. P. Shukla, Phys. Rev. C **67**, 054607 (2003).
36. M. L. Miller, K. Reygers, S. J. Sanders, P. Steinberg, Annu. Rev. Nucl. Part. Sci. **57**, 205 (2007).
37. Q. Y. Shou, Y. G. Ma, P. Sorensen, A. H. Tang, F. Videbk and H. Wang, Physics Letters B **749**, 215 (2015).
38. R. Nouicer, "Habilitation à Diriger des Recherches", University of Strasbourg, 2013 HDR/N^o 293 https://tel.archives-ouvertes.fr/tel-00925262
39. B. B. Back *et al.* (PHOBOS Collaboration), Phys. Rev. Lett. **91**, 502303 (2003).
40. R. Nouicer *et al.* (PHOBOS Collaboration), AIP Conf. Proc. **842**, 86 (2006).
41. B. Alver *et al.* (PHOBOS Collaboration), Phys. Rev. Lett. **102**, 142301 (2009).
42. S. V. Afanasiev *et al.* (NA49 Collaboration), Phys. Rev. C **66**, 054902 (2002).
43. T. Anticic *et al.* (NA49 Collaboration), Phys. Rev. C **69**, 024902 (2004).
44. K. Aamodt *et al.* (ALICE Collaboration), Phys. Rev. Lett. **105**, 252301 (2010).
45. P. Tribedy, R. Venugopalan, Phys. Lett. B **710**, 125 (2012).
46. D. Kharzeev, M. Nardi, Phys. Lett. B **507**, 121 (2001).
47. A. Kovner and M. Lublinsky, Phys. Rev. D **92**, 034016 (2015).
48. R. Nouicer *et al.* (PHOBOS Collaboration), J. Phys. G **30**, S113 (2004).
49. B.B. Back *et al.* (PHOBOS Collaboration), Phys. Rev. Lett. **93**, 082301 (2004).
50. B.B. Back *et al.* (PHOBOS Collaboration), Phys. Rev. C **72**, 031901(R) (2005).
51. B.B. Back *et al.* (PHOBOS Collaboration), Phys. Rev. C **83**, 024913 (2011).
52. R. Nouicer *et al.* (PHOBOS Collaboration), Nucl. Instrum. Meth. in Physics Research A **461**, 143 (2001).
53. B.B. Back *et al.* (PHOBOS Collaboration), Nucl. Instrum. Meth. in Physics Research A **499**, 603 (2003).
54. T.S. Ullrich, Eur. Phys. J. A **19**, s01 (2004).
55. R. Hagedorm, Supl. A. Nuvo Cimento Vol III **No.2**, 150 (1965).
56. I. G. Bearden *et al.* (BRAHMS Collaboration), Phys. Rev. Lett. **90**, 102301 (2003).
57. A. Andronic *et al.*, Nucl. Phys. A **904-905**, 535c (2013).
58. I. G. Bearden *et al.* (BRAHMS Collaboration), Phys. Rev. Lett. **93**, 102301 (2004).
59. M.M. Aggarwal *et al.* (STAR Collaboration), Phys. Rev. C **83**, 034910 (2011).
60. R. Stock, Proceedings of Science (PoS CPOD2006): **040** (2006).
61. P. Braun-Munzinger, K. Redlich, and J. Stachel, in Quark-Gluon Plasma 3, eds. R. C. Hwa, X. N. Wang (World Scientific, Singapore, 2004), p. 491-599.
62. M. Kliemant, R. Sahoo, T. Schuster, and R. Stock, The Physics of the Quark-Gluon Plasma, Lecture Notes in Physics Volume **785**, 23 (2010).
63. F. Becattini, Nucl. Phys. A **702**, 336 (2002).
64. F. Karsch, E. Laermann, and A. Peikert, Phys. Lett. B **478**, 447 (2000).
65. U. Heinz, and G. Kestin, Proceedings of Science (PoS CPOD2006) : **038** 2006.
66. H. Stöcker, J.A. Maruhn, and W. Greiner, Phys. Rev. Lett. **44**, 725 (1980).
67. H. Stöcker, LP Csernai, G. Graebner, G. Buchwald, H. Kruse, RY Cusson, J. A. Maruhn, and W. Greiner, Phys. Rev. C **25**, 1873 (1982).

68. H.Stöcker, and W.Greiner. *et al.*, Phys. Rep. **137**, 277 (1986).
69. W. Reisdorf and H. G. Ritter, Annu. Rev. Nucl. Part. Sci. **47**, 663 (1997).
70. C. Alt *et al.* (NA49 Collaboration), Phys. Rev. C **68**, 034903 (2003).
71. R. Nouicer *et al.* (PHOBOS Collaboration), J. Phys. G **34**, S887 (2007).
72. B. Alver *et al.* (PHOBOS Collaboration), Phys. Rev. Lett. **94**, 122303 (2005).
73. B. Alver *et al.* (PHOBOS Collaboration), Phys. Rev. Lett. **98**, 242302 (2007).
74. A. M. Poskanzer, and S. A. Voloshin, Phys. Rev. C **58**, 1671 (1998).
75. B. Alver, and G Roland, Phys. Rev. C **81**, 054905 (2010).
76. L .X. Han, G. L. Ma, Y. G. Ma, X. Z. Cai, J. H. Chen, and S. Zhang, Phys. Rev. C **84**, 064907 (2011).
77. T. Hirano, U. Heinz, D. Kharzeev, R. Lacey, and Y. Nara, Phys. Lett. B **636**, 299 (2006).
78. Lie-Wen Chen, and Che Ming Ko, Phys. Lett. B **634**, 205 (2006).
79. A. Andronic *et al.* (FOPI Collaboration), Phys. Lett. B **612**, 173 (2005).
80. R. Nouicer *et al.* (PHOBOS Collaboration), Word Scientific, Proceeding of the 22$^{\rm nd}$ Lake Louise Winter Institute, Fundamental Interactions, 373 (2007).
81. N. Borghini and U. A. Wiedemann, J. Phys. G **35**, 023001 (2008).
82. K. Aamodt *et al.* (ALICE Collaboration), Phys. Rev. Lett. **105** 252302 (2010).
83. R. Snellings *et al.* (ALICE Collaboration), J. Phys. G: Nucl. Part. Phys. **38**, 124013 (2011).
84. Md. Nasim *et al.* (STAR Collaboration), Nucl. Phys. A **904**, 413c (2013).
85. J. Adams *et al.* Phys. Lett. B **612**, 181 (2005).
86. J. Adams *et al.* Nucl. Phys. A **757**, 102 (2005).
87. J. Adams *et al.* (STAR Collabortion), Phys. Rev. Lett. **95**, 122301 (2005).
88. J. Adams *et al.* (STAR Collabortion), Phys. Rev. C **77**, 054901 (2008).
89. K. Aamodt *et al.* (ALICE Collaboration), Journal of High Energy Physics **06**, 190 (2015).
90. S.S. Adler *et al.* (PHENIX Collaboration), Phys. Rev. C. **89**, 034915 (2014).
91. C. Gale, S. Jeon, B. Schenke, P. Tribedy, and R. Venugopalan, Phys. Rev. Lett. **110**, 012302 (2013).
92. B. Schenke, P. Tribedy, and R. Venugopalan, Phys. Rev. Lett. **108**, 252301 (2012).
93. B. Schenke, P. Tribedy, and R. Venugopalan, Phys. Rev. C **86**, 034908 (2012).
94. B. Schenke and R. Venugopalan, Phys. Rev. Lett. **113**, 102301 (2014)
95. J. Adams et al. (STAR Collaboration), Phys. Rev. C **72**, 014904 (2005).
96. J. Xu, J. Liao and M. Gyulassy, Chin. Phys. Lett. **32**, 092501 (2015).
97. D. Molnar, S. A. Voloshin, Phys. Rev. Lett. **91**, 092301 (2003).
98. S.S. Adler *et al.* (PHENIX Collaboration), Phys. Rev. Lett. **91**, 072301 (2003).
99. S.S. Adler *et al.* (PHENIX Collaboration), Phys. Rev. Lett. **91**, 241803 (2003).
100. D. d'Enterria, Phys. Lett. B **596**, 32 (2004).
101. J. W. Cronin, H. J. Frisch, M. J. Shochet, J. P. Boymond, P. A. Piroué, and R. L. Sumner, Phys. Rev. D **11**, 3105 (1975).
102. I.G. Bearden *et al.* (BRAHMS Collaboration), Phys. Rev. Lett. **93**, 102301 (2004).
103. B.I. Abelev *et al.* (STAR Collaboration), Phys. Lett. B **655**, 104 (2007).
104. S.S. Adler *et al.* (PHENIX Collaboration), Phys. Rev. Lett. **98**, 172302 (2007).
105. S.S. Adler *et al.* (PHENIX Collaboration), Phys. Rev. Lett. **96**, 202301 (2006).
106. S.S. Adler *et al.* (PHENIX Collaboration), Phys. Rev. Lett. **91**, 072303 (2003).
107. R. Nouicer *et al.* (PHENIX Collaboration), Nucl. Phys. A **862**, 62 (2011).
108. R. Nouicer *et al.* (PHENIX Collaboration), Journal of Physics : Conference Series **420**, 012021 (2013).
109. CMS Collaboration, Eur. Phys. J. C **72**, 1945 (2012).
110. J. D. Bjorken, Phys. Rev. D **27**, 140 (1983).
111. M. Gyulassy *et al.* Phys. Lett. B **243**, 432 (1990).
112. J. J. Gaardhoje *et al.* (BRAHMS Collaboration), Nucl. Phys. A **734**, 13 (2004).
113. M. H. Thoma, and M. Gyulassy *et al.*, Nucl. Phys. B **351**, 491 (1991).
114. A. Accardi and N. Armesto *et al.*, Contribution to the CERN Yellow report on Hard Probes in Heavy Ion Collisions at the LHC (2002).
115. S.S. Alder *et al.* (PHENIX Collaboration), Phys. Rev. Lett. **96**, 032301 (2006).
116. J. Adams *et al.* (STAR Collaboration) , Phys. Rev. Lett. **94**, 062301 (2005).
117. I. Vitev, and Miklos Gyulassy, Nucl. Phys. A **715**, 779 (2003).
118. X. N. Wang, Phys. Lett. B **595**, 165 (2004).
119. I. Vitev, and M. Gyulassy, Phys. Rev. Lett. **89**, 252301 (2002).
120. I. Vitev, J. Phys. G **30**, S791 (2004).
121. M. Banner *et al.* (UA2 Collaboration), Phys. Lett. B **118**, 203 (1982).
122. G. Arnison *et al.* (UA1 Collaboration), Phys. Lett. B **123**, 115 (1983).
123. F. Abe *et al.* (CDF Collaboration), Phys. Rev. Lett. **62**, 613 (1989).
124. F. Abe *et al.* (CDF Collaboration), Phys. Rev. D **41**, 1722 (1990).
125. G. Arnison *et al.* (UA1 Collaboration), Phys. Lett. B **118**, 173 (1982).
126. F. Abe *et al.* (CDF Collaboration), Phys. Rev. Lett. **65**, 968 (1990).
127. T. Akesson *et al.* (Axial Field Spectrometer Collaboration), Phys. Lett. B **123**, 133 (1983).
128. J. A. Appel *et al.* (UA2 Collaboration), Phys. Lett. B **160**, 349 (1985).
129. G. Arnison *et al.* (UA1 Collaboration), Phys. Lett. B **172**, 461 (1986).
130. K. Adcox *et al.* (PHENIX Collaboration), Phys. Rev. Lett. **88**, 022301 (2002).
131. C. Adler *et al.* (STAR Collaboration), Phys. Rev. Lett. **89**, 202301 (2002).
132. P. Jacobs *et al.* (STAR Collaboration), Prog. Nucl. Phys. **54**, 443 (2005).
133. C. Adler *et al.* (STAR Collaboration), Phys. Rev. Lett. **90**, 082302 (2003).

134. J. Adams *et al.* (STAR Collaboration), Phys. Rev. Lett. **91**, 072304 (2003).
135. J. Adams *et al.* (STAR Collaboration), Phys. Rev. Lett. **95**, 152301 (2005).
136. M. Gyulassy, and M. Plümer, Nucl. Phys. A **527**, 641 (1991).
137. X. Wang, and M. Gyulassy,, Phys. Rev. Lett. **68**, 1480 (1992).
138. X. N. Wang, Phys. Rev. C **61**, 064910 (2000).
139. I. Vitev, Phys. Lett. B **562**, 36 (2003).
140. J.w. Qiu, and I. Vitev, Phys. Rev. Lett. **93**, 262301 (2004).
141. D. Kharzeev, E. Levin, and L. McLerran, Phys. Lett. B **561**, 93 (2003).
142. B.B. Back *et al.* (PHOBOS Collaboration), Phys. Rev. Lett. **91**, 072302 (2003).
143. S.S. Adler *et al.* (PHENIX Collaboration), Phys. Rev. Lett. **91**, 072303 (2003).
144. J. Adams *et al.* (STAR Collaboration), Phys. Rev. Lett. **91**, 072304 (2003).
145. I. Arsene *et al.* (BRAHMS Collaboration), Phys. Rev. Lett. **91**, 072305 (2003).
146. M. Gyulassy, I. Vitev, X.N. Wang and B.W. Zhang, Quark Gluon Plasma **3, Eds.** R.C. Hwa and X.-N. Wang, World Scientific, Singapore, p. 123. (2004).
147. S. J. Brodsky, SLAC-PUB-9022.